THERMODYNAMIC AND PHASE-FIELD ANALYSIS OF DOMAIN STRUCTURES AND SWITCHING KINETICS OF BISMUTH FERRITE THIN FILMS

by

RYAN T. HART

Presented to the Faculty of the Graduate School of

The University of Texas at Arlington in Partial Fulfillment

of the Requirements

for the Degree of

MASTER OF SCIENCE

THE UNIVERSITY OF TEXAS AT ARLINGTON

December 2018

Abstract

In this study, thermodynamic analysis and phase-field simulation are utilized to study the polarization, phase transitions, and phase coexistence in BFO thin films. The effect of temperature, substrate strain, and electrical bias on the phase stability and the phase transformation pathways were studied.

Existing thermodynamic analysis methods are supplemented by a phase destrain model, which determines free energy minima as a function of biaxial strain and the fractions of BFO's ferroelectric phases in a thin film. The results of this methodology are compared with phase-field modeling. The phase de-strain model shows reasonable accuracy in determining boundaries at which BFO's phase mixtures and morphotropic phase boundaries can form. Increasing temperature is shown to favor phases that occur at lower strains, and increase the strain required to induce formation of high-strain phases of BFO.

Thermodynamic analysis and phase-field modeling are further used to predict the coercive field and its dependence on the biaxial strain, and temperature. Both models show reasonable agreement. As temperature increases, the coercive field required to induce electrical switching decreases under given substrate strain. Depending on the relative stability of phases at a given strain, the phase transformation can occur as a part of the electrical switching process.

Acknowledgements

First and foremost, I am truly grateful to my research Advisor, Dr. Ye Cao, for his constant support and guidance during my time as his research student. I would also like to thank my labmates, Mr. Yao Ren and Ms. Kena Zhang and my labmates from my previous research group Mr. Owen Abe, and Mr. Mikaeili Fateh. Their feedback and suggestions have helped me better myself as a materials scientist and a researcher. I would also like to thank my committee members Dr. Seong Jin Koh and Dr. Yaowu Hao for their feedback and support, both as part of my dissertation committee and as professors. In both roles, they asked me to further my understanding not just for my own benefit, but to be able to explain it to audiences that were familiar with my line of research and audiences that were not familiar with it.

I am grateful to my classmates and fellow researchers from other lab groups, who both guided me and pushed me to improve throughout my time at UTA. Finally, I would like to thank my parents and brother, who have always pushed me to better myself both as a professional and as a person.

Table of Contents

List of Illustrations

List of Tables

Chapter 1: Introduction

1.1 General Introduction

1.1.1 Ferroelectric perovskites

A ferroelectric is a type of material which possesses a spontaneous polarization that is reversible upon the application of an electric field[1]. Ferroelectric materials have been widely used as sensors, transducers, actuators and acoustic devices, capacitors and non-volatile memory devices. This is due to their switchable polarization, large dielectric permittivity and their unique capability to convert between mechanical and electric energies.

Some of the most promising ferroelectric materials are perovskite crystal ferroelectrics. The general formula of these compounds is ABO_3, where A and B are metal cations, and O represents oxygen atoms. At high temperatures where ferroelectric crystals are grown, ferroelectric materials are in paraelectric state with cubic space group *Pm3m*. The A type cations are located at the corners of the cell, and B type cation is located at the body center of the cell, and the O atoms sit at the face centers of the cell. As a result, the net positive and negative charges coincide with each other at the cell center and cancel with each other. Therefore the crystals tends to be non-polar[1.] When the temperature is below a critical value, typically referred to as the "Curie Temperature", the ferroelectric materials undergo a phase transition from paraelectric to ferroelectric phase. During the phase transition, the B atom displaces from the center of the cell, and the net positive and negative charge no longer coincide with each other. This creates a dipole moment (p), which is equal to the product of the net charge (q) and the distance between the positive and negative charges (l), i.e., $p=ql$, and eventually a spontaneous polarization ($P = \sum_i p_i$). The spontaneous polarization is usually not uniformly aligned along a single direction in an entire

ferroelectric material. The regions where polarizations are uniformly aligned are called ferroelectric domains, and the boundaries separating different ferroelectric domains are named "domain walls". This can lead to the formation of a multi-domain state, as symmetrically related orientations of the crystal may be energetically identical, or degenerate. As a result, these domains are equally likely to form, and can often coexist in a stable structure.

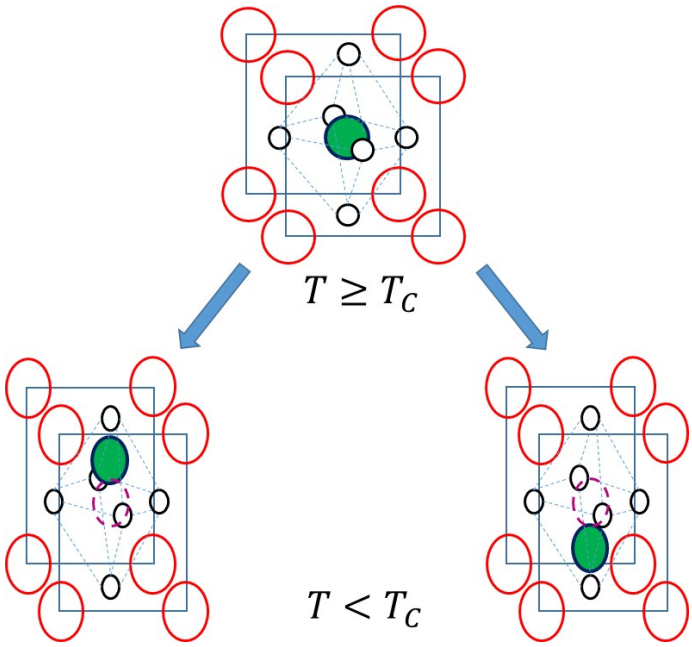

Figure 1. 1: Paraelectric (top) and ferroelectric (bottom) domains of a perovskite unit cell

The paraelectric to ferroelectric transition is often accompanied by an elastic distortion of the unit cell along the direction of the polarization. The coupling between the electric polarization and spontaneous strain (ε_{ij}^0) is described by the electrostrictive coefficient tensor (Q_{ijkl}), i.e.,

$$\varepsilon_{ij}^0 = Q_{ijkl} P_k P_l \tag{1.1}$$

The coupling between strain and electric polarization offers ferroelectric perovskites a wide array of applications in energy conversion devices, and opens up the possibility of tuning ferroelectric properties by external stress/strain, also known as strain engineering.

Another important characteristics of ferroelectric perovskites is that the spontaneous polarization can be switched under an applied electric field among different orientations that are energetically equivalent. For example, in $PbTiO_3$, a prototype ferroelectric oxides, the ferroelectric polarizations can be poled by an externally applied positive electric field from the multi-domain state into a single domain, with polarization aligned along [001] direction. When this positive electric field is removed, the polarization state remains stable until a negative electric field is able to switch it into $[00\bar{1}]$ orientations. The threshold of the electric field when "polarization switching" occurs is called the coercive field. The net polarization change with the applied bi-polar electric field is called the PE hysteresis loop.

Ferroelectricity is one kind of ferroic order. Ferroic orders include ferroelectricity, ferromagnetism, and ferroelasticity, which possess spontaneous polarization, magnetization, and strain respectively. Materials that possess more than one of these properties are known as multiferroics. Multiferroics have seen a wide array of research due to their wide range of physical properties, as well as the complex interactions between them[2 3 4]. These properties can lead to a variety of novel applications for these materials, such as tunnel junctions [5] ferroelectric memory[6] and tunable dielectricity[7].

1.1.2 Bismuth Ferrite

1.1.2.1 BFO *Rhombohedral* phase

Bismuth Ferrite ($BiFeO_3$, or BFO) is a multiferroic perovskite material exhibiting both ferroelectricity (Curie Temperature $T_c \sim 850$ °C) and antiferromagnetism (Neel Temperature $T_N \sim 310$ °C). BFO is a rhomobohedrally-distorted perovskite, with Bi atoms at the cell corners, Fe atom

at the body center and O atoms at the face centers. The unit cell parameters of $BiFeO_3$ are α_r=0.6° and a_p=3.96 Å at room temperature. The spontaneous polarization of bulk rhombohedral phase (*R* phase) is P_s~ 6-7 μC/cm^2 [8]. However, it was discovered that thin films of BFO possessed P_s values nearly an order of magnitude higher than their bulk counterparts (50-60 μC/cm^2). Soon after, it was demonstrated that the high values of P_s are an intrinsic property of BFO's *rhombohedral* phase, with high-purity single-crystal P_s values of roughly 100 μC/cm^2 [9]. In thin films, BFO is observed to undergo monoclinic distortion, although the magnitude of polarization does not significantly change. This implies that strain does not have a direct effect on the material's polarization, consistent with BFO's relatively low piezoelectric coupling [10]. The distorted BFO rhombohedral phase in thin films is occasionally referred to as a separate phase[11]. For the purposes of this work, both the bulk phase and its distorted thin film variant will be referred to as rhombohedral phase (*R* or *R-Like*).

The spontaneous polarization present in *R-like* BFO is located along the pseudocubic cell diagonals, i.e., the $[111]_p$ direction, where subscript "p" denotes the pseudocubic perovskite cell axes. This leads to 8 symmetry-related phase variants, i.e.:

$$r_1^+ = [1,1,1], r_2^+ = [\bar{1},1,1], r_3^+ = [\bar{1},\bar{1},1], r_4^+ = [1,\bar{1},1]$$

$$r_1^- = [\bar{1},\bar{1},\bar{1}], r_2^- = [1,\bar{1},\bar{1}], r_3^- = [1,1,\bar{1}], r_4^- = [\bar{1},1,\bar{1}]$$

These are referred to as "domains" of a crystal, and can be related to one another by rotation about an axis or mirroring about a plane. These domains introduce inhomogeneity to the mechanical and electrical properties of the system, and as a result, induce the formation of domain walls to mediate the change in these properties across domains.

For rhombohedral BFO, there exist three types of domain walls: 71°, 109°, and 180°, which divide domains with reversals of one, two, or three polarization components, respectively. The rhombohedral axes of the domains divided by the 71° and 109° walls are reversed along with their respective polarizations, which leads to an additional ferroelastic reversal[12] whereas the 180° domain walls separate antiparallel domains and thus, do not switch ferroelastic states[13].

1.1.2.2 BFO Monoclinic phases and Morphotropic Phase Boundary

Although the parent ground state of BFO is rhombohedral distorted perovskite, another phase of BFO has been predicted to produce an enormous value of P_s [14], potentially upwards of 150 μC/cm^2. While initially predicted to be tetragonal (*P*4*mm*) [10 15], this phase was discovered to have multiple monoclinic variants: a monoclinically distorted rhombohedral (M_A) structure, and a monoclinically distorted tetragonal (M_c) structure[16 17 18], each with an in-plane polarization components along either {100} (M_C) or {110} (M_A) orientations. These phases possess an expanded unit cell volume and a much larger axial ratio of lattice parameters (*c/a* ~1.23), where *c* and *a* are the in-plane and out-of-plane lattice constants), which is commonly associated with large polarizations[17]. These phases were observed to follow a structural evolution with respect to increasing temperature: $M_C \rightarrow M_A \rightarrow P4mm$[19]. Further studies discovered a method to produce these highly polarized phase of BFO by growing BFO thin films on $LaAlO_3$ (LAO) and $YAlO_3$ (YAO) substrates which yield -4.5% and -6.8% compressive strains [17 20]. At compressive strains of ~4.3% and sufficient film thickness, BFO forms a mixture of the distorted *R* phase and M_C phase. The morphology of the R/M_C mixed phase has been characterized by Atomic Force Microscopy (AFM) and Transmission Electron Microscopy (TEM)[2], which shows an alternating *R* and M_C striped pattern with spacing of 30~50nm and a peak-to-valley height distance of 1~2nm,

as seen in Figures 1.2 and 1.3. This reveals a morphotropic phase boundary (MPB) mediated by the system's in-plane strain.

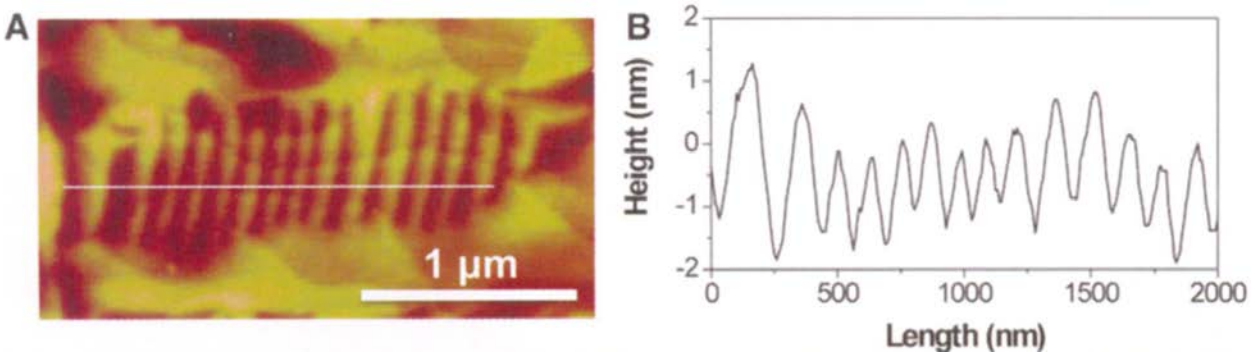

Figure 1. 2:(A) AFM image of BFO's MPB, consisting of alternating R-phase and M_C phase BFO. (B) Height variation of BFO along the MPB. (From [20])

Figure 1. 3: TEM image of BFO's MPB. Light areas correspond to T-phase and dark areas to R-phase. (From [20])

A morphotropic phase boundary is a region that exists between two distinct phases of a material. In this region, since the boundaries between the phases cannot be related by symmetry, the crystal structure changes abruptly (typically from rhombohedral to tetragonal symmetry), which leads to electromechanical properties completely unique to this region[21]. One such material is $Pb(Zr_xTi_{1-x})O_3$, or PZT, which exhibits incredible piezoelectric properties at its MPB composition (x=0.47). Unlike PZT, BFO's MPB does not require stoichiometric modification, and can be created simply by the addition of compressive strain. The MPBs present in BFO display elastic softening[22] and distinct electronic conductivity[23]. Since the formation of MPB's rely on the narrow range of energetic coexistence between the two phases, understanding the effects of external constraints and their role in forming these structures is highly important to developing

their applications. The existence of these highly polarized and switchable phases has prompted a new wave of research on BFO.

Several methods have been utilized to stabilize the highly polar ferroelectric phases of BFO. One such method is “strain engineering”. Strain engineering refers to the selective choice of a substrate material to induce lattice mismatch in a thin film[24]. Due to length mismatch between each material’s lattice parameter, tensile or compressive strain can be induced in the thin film. Application of a compressive strain to a ferroelectric perovskite tends to favor the formation of out-of-plane polarizations [001] while tensile strain favors in-plane polarization [100] or [010], as seen in temperature/strain phase diagrams for many perovskite ferroelectrics[7 10 25]. Several different cubic or pseudocubic materials have been tested as thin film substrates, each imparting a different in-plane strain depending on their lattice parameters. Mixed phase structures (consisting of *R-like* and M_C *–like* BFO) can be produced under specific ranges of biaxial strain through strain engineering, and can be reversibly converted to and from the pure M_C phase by applying an electric field[20]. Thus, extensive control over both the phases and polarizations of a ferroelectric system can be achieved under proper strain engineering, including the creation of MPBs.

1.1.3 Theoretical Analysis

The wide range of properties of BFO have also led to difficulty determining and conducting experiments on the material, as the decomposition of the material and growth of parasitic phases under experimental stimuli can complicate testing the material’s intrinsic properties[6]. As a result, more time and resource-efficient methods of analysis are required to comprehensively analyze or predict a material’s properties. The numerous factors involved in domain stability of multiferroics enable multiple analysis techniques to model specific properties of a material, from using first-

principles calculations to determine the most stable configurations of phases[2 18 19 27] to predicting its electric or magnetic properties through the physical mechanisms of its crystal structure[16]. These methods have been instrumental in determining the relative stability of the ferroelectric phases of BFO, as well as the properties they can exhibit. To build on this, theoretical modeling has been utilized as an effective way to predict minimum energy configurations of materials[6], as well as short range order over several unit cells [20].

1.1.3.1 Thermodynamic analysis

A crystal can be considered as "a thermodynamic system whose equilibrium state can be completely specified by the values of a number of variables. The internal energy of the system can be expressed as a function of the mechanical and electrical strains in addition to temperature"[1]. Therefore, this methodology, referred to as a "thermodynamic model" can represent the various electrical and mechanical constraints of a crystal system and define the free energy density of its phases as a function of these constraints. By minimizing the total free energy density, the equilibrium structure of a material can be determined for any combination of internal or external constraints.

Direct thermodynamic analysis by modeling free energy density of a system has been utilized to predict phase transitions and phase stability for ferroelectric materials[25 28 29 30]. These analysis methods apply the contributions from multiple sources of energy to Helmholtz free energy density (F_{BFO}) to construct phase diagrams of ferroelectric materials. By adding mechanical constraints to approximate thin-film boundary conditions, this thermodynamic approach can approximate F_{BFO} of idealized ferroelectric phases. This approach demonstrates reasonable

accuracy in determining the ferroelectric phases under both thermal and mechanical constraints, and can even be expanded to determine the relative stability of multiple phases of a material.

The value of F_{BFO} for each stable phase is a function of both the temperature and strain of the system. In a one-dimensional (1D) thin film system, the phases of system do not intersect each other (i.e. each domain is distinct) and the process of epitaxial growth conserves the total deformation of the system. In a system where total deformation is conserved, the fractions of each phase may be treated as functions of their respective strains. Thus the overall strain may be expressed as follows:

$$\varepsilon^0 = f^\alpha \varepsilon^\alpha + f^\beta \varepsilon^\beta \quad (1.2)$$

Where *f* is the fraction of each distinct phase, and ε is the individual strain of each phase. If the phase fraction f^β is treated as 1-f^α (as $f^\alpha + f^\beta = 1$), then (1.2) can be rewritten in terms of f^α or ε^β:

$$f^\alpha = \frac{\varepsilon^\beta - \varepsilon^0}{\varepsilon^\beta - \varepsilon^\alpha} \leftrightarrow \varepsilon^\beta = (\varepsilon^0 - f^\alpha \varepsilon^\alpha)/(1 - f^\alpha) \quad (1.3)$$

Thus, if $\varepsilon^\beta = \varepsilon^0$, then the structure will be entirely β phase, and vice-versa. The strains associated with each phase can be considered their "critical strain", or strain required to induce a "pure" phase. Thus, if a variable is a function of the in-plane strain of the system, it can be defined as follows:

$$F_{BFO}(\varepsilon^0) = f^\alpha F^\alpha{}_{BFO}(\varepsilon^\alpha) + f^\beta F^\beta{}_{BFO}(\varepsilon^\beta) \quad (1.4)$$

Where the strain energy of an individual phase is treated as:

$$f^\alpha F^\alpha{}_{BFO}(\varepsilon^\alpha) = \varepsilon^\alpha \sigma^\alpha \quad (1.5)$$

Minimizing the free energy with respect to a phase's strain finds:

$$\frac{\partial F_{BFO}(\varepsilon^0)}{\partial \varepsilon^\alpha} = f^\alpha \frac{\partial F^\alpha{}_{BFO}(\varepsilon^\alpha)}{\partial \varepsilon^\alpha} + (1 - f^\alpha) \frac{\partial F^\beta{}_{BFO}(\varepsilon^\beta)}{\partial \varepsilon^\alpha} = 0 \tag{1.6}$$

Since the total deformation of the system is a function of both phase's strains:

$$\frac{\partial F^\beta{}_{BFO}(\varepsilon^\beta)}{\partial \varepsilon^\alpha} = \frac{F^\beta{}_{BFO}(\varepsilon^\beta))}{\partial \varepsilon^\beta} \frac{\partial \varepsilon^\beta}{\partial \varepsilon^\alpha} \tag{1.7}$$

Where:

$$\frac{\partial \varepsilon^\beta}{\partial \varepsilon^\alpha} = \frac{-f^\alpha}{1-f^\alpha} \tag{1.8}$$

Solving for the minima of the free energy as a function of strain gives us:

$$\frac{\partial F_{BFO}(\varepsilon^0)}{\partial \varepsilon^\alpha} = f^\alpha \frac{\partial F^\alpha{}_{BFO}(\varepsilon^\alpha)}{\partial \varepsilon^\alpha} + \cancel{(1 - f^\alpha)} \frac{\partial F^\beta{}_{BFO}(\varepsilon^\beta)}{\partial \varepsilon^\beta} \frac{-f^\alpha}{\cancel{1-f^\alpha}} = 0 \tag{1.9}$$

$$\rightarrow f^\alpha \frac{\partial F^\alpha{}_{BFO}(\varepsilon^\alpha)}{\partial \varepsilon^\alpha} + (-f^\alpha) \frac{\partial F^\beta{}_{BFO}(\varepsilon^\beta)}{\partial \varepsilon^\beta} = 0 \rightarrow \frac{\partial F^\alpha{}_{BFO}(\varepsilon^\alpha)}{\partial \varepsilon^\alpha} = \frac{\partial F^\beta{}_{BFO}(\varepsilon^\beta)}{\partial \varepsilon^\beta} \tag{1.10}$$

Thus, at equilibrium, the stress of the system is uniform for each phase. Minimizing the system's free energy with respect to the phase fraction gives:

$$\frac{\partial F_{BFO}(\varepsilon^0)}{\partial f^\alpha} = f^\alpha \frac{\partial F^\alpha{}_{BFO}(\varepsilon^\alpha)}{\partial f^\alpha} + (1 - f^\alpha) \frac{\partial F^\beta{}_{BFO}(\varepsilon^\beta)}{\partial f^\alpha} = 0 \tag{1.11}$$

Since:

$$\frac{\partial F_{BFO}(\varepsilon^\beta)}{\partial f^\alpha} = \frac{\partial F_{BFO}(\varepsilon^\beta)}{\partial \varepsilon^\beta} \frac{\partial \varepsilon^\beta}{\partial f^\alpha} \tag{1.12}$$

Where:

$$\frac{\partial \varepsilon^{\beta}}{\partial f^{\alpha}} = -\frac{\partial \varepsilon^{\beta}}{\partial f^{\beta}} \tag{1.13}$$

(1.11) becomes:

$$\frac{\partial F_{BFO}(\varepsilon^0)}{\partial f^{\alpha}} = F^{\alpha}{}_{BFO}(\varepsilon^{\alpha}) - F^{\beta}{}_{BFO}(\varepsilon^{\beta}) + (\varepsilon^{\beta} - \varepsilon^{\alpha})\frac{\partial F^{\beta}{}_{BFO}(\varepsilon^{\beta})}{\partial \varepsilon^{\beta}} = 0 \tag{1.14}$$

$$\rightarrow \frac{\partial F^{\alpha}{}_{BFO}(\varepsilon^{\alpha})}{\partial f^{\alpha}} = \frac{\partial F^{\beta}{}_{BFO}(\varepsilon^{\beta})}{\partial f^{\beta}} = \frac{F^{\alpha}{}_{BFO}(\varepsilon^{\alpha}) - F^{\beta}{}_{BFO}(\varepsilon^{\beta})}{(\varepsilon^{\alpha} - \varepsilon^{\beta})} \tag{1.15}$$

Thus, the tangent lines of each phase fraction's free energy density (with respect to their strain) are common at equilibrium[31]. These conditions can be used to determine the lowest free energy states for a phase combination as a function of strain. The Gibbs free energy density of each phase can be related to the Helmholtz free energy density by the Legendre Transformation[30]:

$$G^{\alpha}{}_{BFO}(\varepsilon^{\alpha}) = F^{\alpha}{}_{BFO}(\varepsilon^{\alpha}) - \varepsilon^{\alpha}\frac{\partial F^{\alpha}{}_{BFO}(\varepsilon^{\alpha})}{\partial \varepsilon^{\alpha}} = G^{\beta}{}_{BFO}(\varepsilon^{\beta}) = F^{\beta}{}_{BFO}(\varepsilon^{\beta}) - \varepsilon^{\beta}\frac{\partial F^{\beta}{}_{BFO}(\varepsilon^{\beta})}{\partial \varepsilon^{\beta}} \tag{1.16}$$

The chemical potential of a phase is related to the Gibb's Free energy of a 1D substance by:

$$\mu^{\alpha} = f^{\alpha} G^{\alpha}{}_{BFO}(\varepsilon^{\alpha}) \tag{1.17}$$

From (1.2) and (1.17), it is clear that strain's relationship with Helmholtz Free energy is analogous to chemical potential's relationship with Gibb's Free energy, as seen in Figure 1.4. As a result, it is possible to determine the phase fraction of a substance as a function of its strains, as in (1.3), thus forming a strain-driven "lever rule".

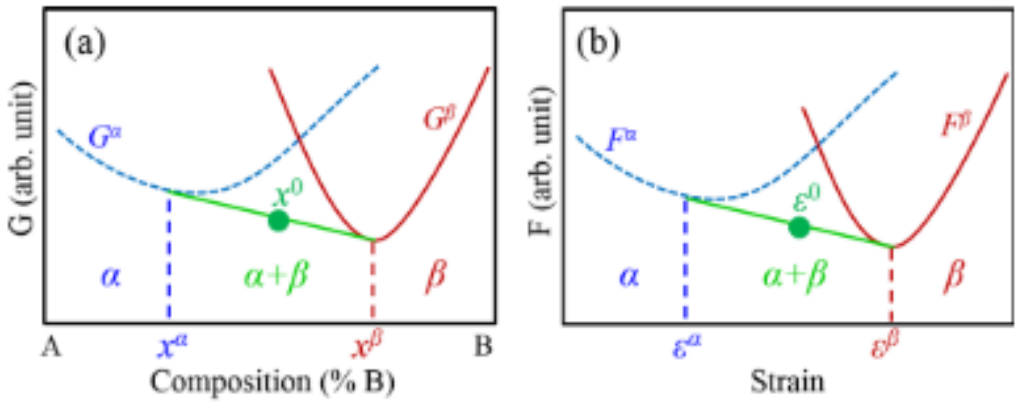

Figure 1. 4: Composition and Strain phase separation - Common Tangent Construction (From [30])

1.1.3.2 Phase-field Method

Phase-field modeling has emerged as a powerful method for modeling the microstructures and their evolutions in many materials. A phase field "describes a microstructure (both compositional/structural domains and interfaces) as a whole by using field variables which are continuous across the interfacial regions." [32]. Typical examples of field variables include the grain orientations describing a grain structure, the spontaneous polarization describing ferroelectric domain structure, the concentration of an equilibrium phase during the phase transformation process (such as solidification), etc. Like thermodynamic analysis, phase-field modeling defines the free energy of the system as a function of thermodynamic and kinetic variables. From an initially defined set of field variables (either from a preset structure or randomized values), the energy of the system is iteratively solved for at each point in a defined simulation space as a function of time until an equilibrium structure is reached. Unlike thermodynamic analysis, the free energy of individual phases and domains is solved with respect to both space and time, allowing implementation of energy terms dependent on the polarization gradient, such as domain walls, and

the time-dependent kinetic evolution of a field variable. As a result, phase-field modeling can determine the free energy of individual domains, as well as the domain walls that mediate their properties. This method has been used to great success to model the phase formation of multiple ferroelectric materials as a function of their polarization [24 33].

1.1.4 Motivation

Until now, many studies of BFO have focused on the intrinsic ferroelectric properties of BFO, or analyzed effects of strain-engineering on BFO at room temperature. However, few studies have investigated the impact of increasing temperatures on domain formation and domain preference of BFO films, aside from notable transition temperatures, like the Neel and Curie temperatures[34 35]. On the other hand, the polarization switching under an applied electric field is strongly coupled with the local strain state. Due to the complexity of mixed phase region of BFO under large compressive strain, the switching processes become even more complicated. Therefore, both systematic analysis and fundamental understanding of field-driven polarization rotation and switching dynamics in BFO's single and mixed phase structures is highly important. Since these properties can have a tremendous impact on the formation of MPBs, displaying their contributions in a comprehensive model can improve the research of BFO's strain-driven MPB.

1.2 Research Objective

The goal of this thesis is to fundamentally understand the phase transitions, domain structure, and domain switching process in BFO ferroelectric thin film. The specific objectives are:

(1) Develop a thermodynamic analysis method to predict phase formation under strain-temperature conditions in BFO.

(2) Create a comprehensive strain-temperature phase diagram for BFO, using both phase-field modeling and thermodynamic analysis, and determine the differences between these methods.

(3) Determine the electrical switching behavior of BFO thin film by investigating the polarization rotations and the new phase formation, and its dependence on strain and temperature.

1.3 Theoretical Structure

This thesis is organized into 5 chapters.

Chapter 1 presents a general introduction of the basic concepts of ferroelectric perovskites, the crystal structure and properties of bismuth ferrite, the strain-tuned morphotropic phase boundary, and the existing thermodynamics and phase-field approaches to ferroelectric materials. This is followed by the motivation, the research objectives, and the structure of this thesis.

Chapter 2 presents the methodology used to analyze BFO's thin film domain formation as a function of strain and temperature by both thermodynamic analyze and phase-field modeling. The thermodynamic model is presented in terms of its energy density as well as its boundary conditions, both for single phase and mixed phase analysis. The phase-field model is presented in terms of its energy density and physical parameters, in addition to the phase-field simulation process.

In chapter 3, both thermodynamic analysis and phase-field modeling are applied to study effects of strain and temperature on the properties and free energy of BFO's ferroelectric domains.

In addition, the relative stability of each phase, as well as the stability of mixed phase regions, are determined. A strain-temperature diagram of BFO's phase formation is developed.

In chapter 4, thermodynamic analysis is applied to study the electrical switching behavior of BFO thin film single domains under multiple strain and temperature conditions. Phase-field modeling is applied to study the PE hysteresis behavior of BFO's domains under multiple strain and temperature conditions. The results obtained from the two theoretical models are compared.

Chapter 5 presents the conclusions of this work and discussion on future directions of BFO domains characterization and study.

References

[1] Jona, F. and Shirane, G. *Ferroelectric Crystals.* 6-15 (Pergamon Press Inc.,1962).

[2] Lubk, A., Gemming, S. & Spaldin, N. A. First-principles study of ferroelectric domain walls in multiferroic bismuth ferrite. *Phys. Rev. B - Condens. Matter Mater. Phys.* **80,** 1–8 (2009).

[3] Seidel, J. *et al.* Conduction at domain walls in oxide multiferroics. *Nat. Mater.* **8,** 229–234 (2009).

[4] Ramesh, R. & Spaldin, N. A. Multiferroics: progress and prospects in thin films. *Nat. Mater.* **6,** 21–29 (2007).

[5] Sando, D., Xu, B., Bellaiche, L. & Nagarajan, V. A multiferroic on the brink: Uncovering the nuances of strain-induced transitions in $BiFeO_3$. *Appl. Phys. Rev.* **3,** 011106 (2016).

[6] Catalan, G. & Scott, J. F. Physics and Applications of Bismuth Ferrite. *Adv. Mater.* **21,** 2463–2485 (2009).

[7] Schlom, D. G. *et al.* Elastic strain engineering of ferroic oxides. *MRS Bull.* **39,** 118–130 (2014).

[8] Wang, J. *et al.* Epitaxial $BiFeO_3$ multiferroic thin film heterostructures. *Science (80-.).* **299,** 1719–1722 (2003).

[9] Lebeugle, D. *et al.* Room-temperature coexistence of large electric polarization and magnetic order in $BiFeO_3$ single crystals. *Phys. Rev. B - Condens. Matter Mater. Phys.* **76,** 1–8 (2007).

[10] Ederer, C. & Spaldin, N. A. Effect of epitaxial strain on the spontaneous polarization of thin film ferroelectrics. *Phys. Rev. Lett.* **95,** 2–5 (2005).

[11] Beekman, C. *et al.* Phase Transitions, Phase Coexistence, and Piezoelectric Switching Behavior in Highly Strained $BiFeO_3$ Films. *Adv. Mater.* **25,** 5561–5567 (2013).

[12] Zhao, T. *et al.* Electrical control of antiferromagnetic domains in multiferroic $BiFeO_3$ films at room temperature. *Nat. Mater.* **5,** 823–829 (2006).

[13] Baek, S. H. *et al.* Ferroelastic switching for nanoscale non-volatile magnetoelectric devices. *Nat. Mater.* **9,** 309–314 (2010).

[14] Yun, K. Y., Ricinschi, D., Kanashima, T., Noda, M. & Okuyama, M. Giant Ferroelectric Polarization Beyond 150 μC/cm 2 in $BiFeO_3$ Thin Film. *Jpn. J. Appl. Phys.* **43,** L647–L648 (2004).

[15] Ricinschi, D., Yun, K.-Y. & Okuyama, M. A mechanism for the 150 μC cm −2 polarization of $BiFeO_3$ films based on first-principles calculations and new structural data. *J. Phys. Condens. Matter* **18,** L97–L105 (2006).

[16] Ravindran, P., Vidya, R., Kjekshus, A., Fjellvåg, H. & Eriksson, O. Theoretical investigation of magnetoelectric behavior in $BiFeO_3$. *Phys. Rev. B* **74,** 224412 (2006).

[17] Béa, H. *et al.* Evidence for room-temperature multiferroicity in a compound with a giant axial ratio. *Phys. Rev. Lett.* **102,** 1–5 (2009).

[18] Diéguez, O., González-Vázquez, O. E., Wojdeł, J. C. & Íñiguez, J. First-principles predictions of low-energy phases of multiferroic $BiFeO_3$. *Phys. Rev. B* **83,** 094105 (2011).

[19] Liu, H.-J. *et al.* Structural study in highly compressed $BiFeO_3$ epitaxial thin films on YAlO 3. *J. Appl. Phys.* **112,** 052002 (2012).

[20] Zeches, R. J. *et al.* A Strain-Driven Morphotropic Phase Boundary in $BiFeO_3$. *Science (80-.).* **326,** 977–980 (2009).

[21] Ahart, M. *et al.* Origin of morphotropic phase boundaries in ferroelectrics. *Nature* **451,** 545–548 (2008).

[22] Li, Q. *et al.* Giant elastic tunability in strained $BiFeO_3$ near an electrically induced phase transition. *Nat. Commun.* **6,** 8985 (2015).

[23] Sharma, P. *et al.* Structural and electronic transformation pathways in morphotropic $BiFeO_3$. *Sci. Rep.* **6,** 32347 (2016).

[24] Schlom, D. G. *et al.* Strain Tuning of Ferroelectric Thin Films. *Annu. Rev. Mater. Res.* **37,** 589–626 (2007).

[25] Koukhar, V. G., Pertsev, N. A. & Waser, R. Thermodynamic theory of epitaxial ferroelectric thin films with dense domain structures. *Phys. Rev. B* **64,** 214103 (2001).

[26] Diéguez, O., Aguado-Puente, P., Junquera, J. & Íñiguez, J. Domain walls in a perovskite oxide with two primary structural order parameters: First-principles study of $BiFeO_3$. *Phys. Rev. B* **87,** 024102 (2013).

[27] Cazorla, C. & Íñiguez, J. Insights into the phase diagram of bismuth ferrite from quasiharmonic free-energy calculations. *Phys. Rev. B* **88,** 214430 (2013).

[28] Shih, W. Y., Shih, W.-H. & Aksay, I. A. Size dependence of the ferroelectric transition of small $BaTiO_3$ particles: Effect of depolarization. *Phys. Rev. B* **50,** 15575–15585 (1994).

[29] Iniguez, J., Ivantchev, S., Perez-Mato, J. M. & Garcia, A. Devonshire-Landau free energy of $BaTiO_3$ from first principles. *Phys. Rev. B* **63,** 144103 (2000).

[30] Xue, F., Li, Y., Gu, Y., Zhang, J. & Chen, L.-Q. Strain phase separation: Formation of ferroelastic domain structures. *Phys. Rev. B* **94,** 220101 (2016).

[31] Xue, F., Ji, Y. & Chen, L.-Q. Theory of strain phase separation and strain spinodal: Applications to ferroelastic and ferroelectric systems. *Acta Mater.* **133,** 147–159 (2017).

[32] Chen, L.-Q. Phase-Field Models for Microstructure Evolution. *Annu. Rev. Mater. Res.* **32,** 113–140 (2002).

[33] Chen, L. Q. Phase-field method of phase transitions/domain structures in ferroelectric thin films: A review. *J. Am. Ceram. Soc.* **91,** 1835–1844 (2008).

[34] Infante, I. C. *et al.* Bridging multiferroic phase transitions by epitaxial strain in $BiFeO_3$. *Phys. Rev. Lett.* **105,** 057601 (2010).

[35] Sando, D. *et al.* Control of ferroelectricity and magnetism in multi-ferroic $BiFeO_3$ by epitaxial strain. *Philos. Trans. R. Soc. A Math. Phys. Eng. Sci.* **372,** 20120438–20120438 (2014).

Chapter 2: Methodology

2.1 Thermodynamic Analysis

2.1.1 Solution of Simultaneous equations for single-phase BFO

To better understand the contributions of external input to phase stability, F_{BFO} is split into two components: Landau, Elastic. The Landau and Elastic energy Coefficients were supplied by literature[1]. The Landau, or bulk energy, represents the most energetically stable configurations of the system without any external inputs. The expanded Landau portion of the system is as follows:

$$f_{Landau} = \alpha_{11} * \left(P_x{}^2 + P_y{}^2 + P_z{}^2\right) + \alpha_{1111} * \left(P_x{}^4 + P_y{}^4 + P_z{}^4\right) + \alpha_{1122}\left(P_x{}^2P_y{}^2 + P_x{}^2P_z{}^2 + P_y{}^2P_z{}^2\right) + \alpha_{111111} * \left(P_x{}^6 + P_y{}^6 + P_z{}^6\right) + \alpha_{111122}\left(P_x{}^4\left(P_y{}^2 + P_z{}^2\right) + P_y{}^4\left(P_x{}^2 + P_z{}^2\right) + P_z{}^4\left(P_x{}^2 + P_y{}^2\right)\right) + \alpha_{112233} * \left(P_x{}^2 * P_y{}^2 * P_z{}^2\right) + \alpha_{11111111} * \left(P_x{}^8 + P_y{}^8 + P_z{}^8\right) + \alpha_{11111122}\left(P_x{}^6\left(P_y{}^2 + P_z{}^2\right) + P_y{}^6\left(P_x{}^2 + P_z{}^2\right) + P_z{}^6\left(P_x{}^2 + P_y{}^2\right)\right) + \alpha_{11112222} * \left(\left(P_x{}^4P_y{}^4\right) * \left(P_y{}^4P_z{}^4\right) * \left(P_x{}^4P_z{}^4\right)\right) + \alpha_{11112233}\left(P_x{}^4\left(P_y{}^2 * P_z{}^2\right) + P_y{}^4\left(P_x{}^2 * P_z{}^2\right) + P_z{}^4\left(P_x{}^2 * P_y{}^2\right)\right) \quad (2.1)$$

All Landau energy coefficients are considered constant, except for α_{11}, which is linearly dependent on temperature, and obeys the Curie-Weiss Law[2]. The Landau energy is expanded to 8th order to correctly represent the monoclinic phases of BFO[3]. For simplicity, the effects of octahedral tilt are neglected.

The Elastic energy represents the effects of the strain induced by the lattice mismatch of the thin film and its substrate, as well as the energy contributions by the strain induced by electrostriction, or the eigenstrain/stress-free strain. The expanded Elastic portion is as follows:

$$f_{Elastic} = {}^1/_2 * \left(c_{66}\left(e_6 - 2 * h_{66}P_xP_y\right)\right)^2 + \left(c_{55}\left(e_5 - 2 * h_{55}P_xP_z\right)\right)^2 + \left(c_{44}\left(e_4 - 2 * h_{44}P_yP_z\right)\right)^2 + \left(e_1 - h_{12}P_y{}^2 - h_{12}P_z{}^2\right) * \left(c_{12}\left(e_3 - h_{12}P_x{}^2 - h_{12}P_y{}^2\right) + c_{12}\left(e_2 - h_{12}P_x{}^2 - h_{12}P_z{}^2\right) + c_{11}\left(e_1 -\right.\right.$$

$h_{12}{P_y}^2 - h_{12}{P_z}^2)\big) + \big(e_2 - h_{12}{P_x}^2 - h_{12}{P_z}^2\big) * \Big(c_{12}\big(e_3 - h_{12}{P_x}^2 - h_{12}{P_y}^2\big) + c_{11}\big(e_2 - h_{12}{P_x}^2 - h_{12}{P_z}^2\big) + c_{12}\big(e_1 - h_{12}{P_y}^2 - h_{12}{P_z}^2\big)\Big) + \big(e_3 - h_{12}{P_x}^2 - h_{12}{P_y}^2\big) * \Big(c_{11}\big(e_3 - h_{12}{P_x}^2 - h_{12}{P_y}^2\big) + c_{12}\big(e_2 - h_{12}{P_x}^2 - h_{12}{P_z}^2\big) + c_{12}\big(e_1 - h_{12}{P_y}^2 - h_{12}{P_z}^2\big)\Big)\big)$ (2.2)

Where e_i are the total strain components of the system, h_{ij} are electrostriction coefficients, and c_{ij} are stiffness coefficients.

Since the paraelectric phase of BFO possesses cubic symmetry[4], the elastic properties of BFO follow cubic symmetry. To approximate the boundary conditions of a thin film, the following constraints were utilized:

$$\varepsilon_{11} = \varepsilon_{22} = \varepsilon_C, \varepsilon_{12} = 0, \frac{\partial F_{BFO}}{\partial \varepsilon_{13}} = 0, \frac{\partial F_{BFO}}{\partial \varepsilon_{23}} = 0, \frac{\partial F_{BFO}}{\partial \varepsilon_{33}} = 0 \quad (2.3)$$

These constraints set the in-plane strains of the system as equal to each other, set in-plane shear strain to 0, and the remaining strain values to be calculated as functions of the in-plane strain.

$$\frac{\partial F_{BFO}}{\partial P_x} = 0, \frac{\partial F_{BFO}}{\partial P_y} = 0, \frac{\partial F_{BFO}}{\partial P_z} = 0, \frac{\partial^2 F_{BFO}}{\partial {P_x}^2} \geq 0, \frac{\partial^2 F_{BFO}}{\partial {P_y}^2} \geq 0, \frac{\partial^2 F_{BFO}}{\partial {P_z}^2} \geq 0, P_x > 0, P_y > 0 \quad (2.4)$$

The first three constraints determined F_{BFO} extremities of the system, and the next three set only the minima of the system to be counted. The final constraints limit the redundant phases of the system. Since all polarization terms in the system are raised to an even-valued exponent, positive and negative variations of polarizations do not affect the magnitude of the free energy, and can thus be simplified to only solve for positive variants of these terms. Since the gradient energy is neglected in this case, the thermodynamic solution can be considered as a solution when domain wall energy has negligible influence, or when the domain wall density is small[1]. All Landau,

elastic, and electrostrictive coefficients are listed in Appendices A and B for thermodynamic and phase-field analysis respectively.

2.1.2 Energy Curve for rhombohedral and monoclinic phases, phase boundary approximation from common tangent construction

Once the free energies for the two phases were determined over a range of compressive strain, 2nd order approximations of their free energy with respect to strain were found from the calculated data. With these free energy curves, the conditions for free energy minima with respect to both strain and the phase fractions of the structure were fulfilled:

$$\frac{F^{\alpha}{}_{BFO}(\varepsilon^{\alpha})}{\partial \varepsilon^{\alpha}} = \frac{F^{\beta}{}_{BFO}(\varepsilon^{\beta})}{\partial \varepsilon^{\beta}} \tag{2.5}$$

$$\frac{F^{\alpha}{}_{BFO}(\varepsilon^{\alpha})}{\partial f^{\alpha}} = \frac{F^{\beta}{}_{BFO}(\varepsilon^{\beta})}{\partial f^{\alpha}} = \frac{F^{\alpha}{}_{BFO}(\varepsilon^{\alpha}) - F^{\beta}{}_{BFO}(\varepsilon^{\beta})}{(\varepsilon^{\alpha} - \varepsilon^{\beta})} \tag{2.6}$$

From this, the critical strains of each phase can be found. Thus, the phase fractions of each phase can be determined from (1.2).

2.1.3 Varying Landau Coefficient by changing temperature

The only temperature-dependent variable in the thermodynamic model is the 2nd order Landau Coefficient, which is defined as[2]:

$$\alpha_{11} = \frac{T - T_C}{\varepsilon_0 C} \tag{2.7}$$

Where ε_0 is the permittivity of free space, and T_C and C are the Curie temperature and Curie constant, respectively. After changing the temperature, a new free energy curve can be constructed for both phases, and the aforementioned "lever-rule" method can be used to determine the critical strains and phase fractions.

2.2 Phase-Field Modeling

2.2.1 Phase-Field Introduction –Time-Dependent Ginzburg Landau equation

Phase-field simulation is utilized to consider additional parameters that could not be easily tested in the "dimensionless" thermodynamic analysis, as well as the evolution of the structure over time. The system is described by the time dependent Ginzburg-Landau (also known as Allen-Cahn) equations, as follows:

$$\frac{\partial P_i(r,t)}{\partial t} = -L\frac{\delta F_{BFO}}{\delta P_i(r,t)}, (i = 1,2,3) \qquad (2.8)$$

Where L is a kinetic parameter related to interface mobility, P is the polarization in terms of direction and time, and F_{BFO} is the Helmholtz free energy functional of the system.[5]. F_{BFO} is defined as a spacial integral of each of its energy terms[6]:

$$F_{BFO} = \int_V [f_{Landau}(P_r) + f_{Elastic}(P_r, \varepsilon_{ij}) + f_{Electric}(P_r, E_{ij}) + f_{Grad}(\nabla P_r)]dV \qquad (2.9)$$

Once the energy of the system is defined, the Allen-Cahn equation can be solved numerically by the semi-implicit Fourier-spectral method[7].

The additional energy parameters are the electrostatic energy and the gradient energy. The electrostatic energy represents the effects of a "homogeneous" electrical field.

$$f_{Electric} = -(E_x * P_x + E_y * P_y + E_z * P_z) - {}^1\!/_2\,\varepsilon_0\kappa_B(E_x{}^2 + E_y{}^2 + E_z{}^2) \qquad (2.10)$$

Where $E_{x,y,z}$ are the electrical field components oriented in Cartesian Coordinates, ε_0 is the permittivity of vacuum, and κ_B is the background dielectric constant[6]. The gradient energy encompasses the domain wall energy of the system. Domain wall energy is only present in the boundaries between different phases, including both phases of alternating polarization polarity, or

phases with different free energy density altogether. The stability and orientation of a domain wall are a function of the electrostatic, elastic, and gradient energies of the domain structures it divides[8]. The gradient energy density used in the phase-field method is detailed as follows:

$$F_{Grad} = \frac{1}{2}G_{11}\left(\frac{dP_x}{dx}^2 + \frac{dP_y}{dy}^2 + \frac{dP_z}{dz}^2\right) + \frac{1}{2}G_{44}(\left(\frac{dP_x}{dy} + \frac{dP_y}{dx}\right)^2 + \left(\frac{dP_y}{dz} + \frac{dP_z}{dy}\right)^2 + \left(\frac{dP_1}{dz} + \frac{dP_z}{dx}\right)^2 +$$

$$\frac{1}{2}G'_{44}(\left(\frac{dP_x}{dy} - \frac{dP_y}{dx}\right)^2 + \left(\frac{dP_y}{dz} - \frac{dP_z}{dy}\right)^2 + \left(\frac{dP_1}{dz} - \frac{dP_z}{dx}\right)^2 \quad (2.11)$$

Where G_{ij} are the gradient energy coefficients. As the gradient energy is dependent on the polarization gradient rather than the magnitude of the polarization, polarity switching's effect on energy increases when the magnitude of polarization increases. As a result, its effects become much more apparent when switching a domain with high magnitude polarization components.

In addition to this, the strain in a phase-field system is not homogeneous, or the strain may vary from one location to another. In order to accommodate for this new factor, strain can be split into homogeneous and heterogeneous components. This is detailed in literature[8].

For domain formation simulation, the phase-field system is defined as a 128x128 nm^2 thin film. For electrical switching, the system is defined as a 64x64 nm^2 thin film to expedite testing. Film thickness is set to 20 nm to minimize the effect of strain relaxation[9]. The substrate thickness is set to roughly 10 nm for all tests. The film is oriented in the [001]-plane. In order to determine the effects of each of the external parameters on phase formation in BFO, each test began with small randomized values for each polarization under a specific strain/temperature condition. Out of plane polarization (P_z) is set to have only positive initial conditions to simulate the "self-poled" effect[1]. No in-plane shear gradient components were considered, as the shear strain is suppressed as part of the thin film boundary conditions.

References

[1] Xue, F., Li, Y., Gu, Y., Zhang, J. & Chen, L.-Q. Strain phase separation: Formation of ferroelastic domain structures. *Phys. Rev. B* **94,** 220101 (2016).

[2] Koukhar, V. G., Pertsev, N. A. & Waser, R. Thermodynamic theory of epitaxial ferroelectric thin films with dense domain structures. *Phys. Rev. B* **64,** 214103 (2001).

[3] Vanderbilt, D. & Cohen, M. H. Monoclinic and triclinic phases in higher-order Devonshire theory. *Phys. Rev. B* **63,** 094108 (2001).

[4] Ricinschi, D., Yun, K.-Y. & Okuyama, M. A mechanism for the 150 μC cm −2 polarization of $BiFeO_3$ films based on first-principles calculations and new structural data. *J. Phys. Condens. Matter* **18,** L97–L105 (2006).

[5] Chen, L.-Q. Phase-Field Models for Microstructure Evolution. *Annu. Rev. Mater. Res.* **32,** 113–140 (2002).

[6] Chen, L. Q. Phase-field method of phase transitions/domain structures in ferroelectric thin films: A review. *J. Am. Ceram. Soc.* **91,** 1835–1844 (2008).

[7] Chen, L. Q. & Shen, J. Applications of semi-implicit Fourier-spectral method to phase field equations. *Comput. Phys. Commun.* **108,** 147–158 (1998).

[8] Li, Y. L., Hu, S. Y., Liu, Z. K. & Chen, L. Q. Effect of substrate constraint on the stability and evolution of ferroelectric domain structures in thin films. *Acta Mater.* **50,** 395–411 (2002).

[9] Chen, Z. *et al.* Nanoscale domains in strained epitaxial $BiFeO_3$ thin Films on $LaSrAlO_4$ substrate. *Appl. Phys. Lett.* **96,** 252903 (2010).

Chapter 3: Results - Strain/Temperature BFO Characterization

3.1 Introduction

Both temperature and strain have been shown to have a profound effect on the phase formation of ferroelectrics. While the effects of temperature[1] and strain[2 3 4] have been investigated independently for BFO, few groups[1 5] have considered them in tandem. The behavior of highly-strained BFO under high temperatures is often limited to relatively low compressive strain values (0-2%)[3 6 7]. As a result, the formation of phases and phase boundaries under wider ranges of strain and temperature remains unexplored. As a result, the free energy densities of BFO's phases as a function of compressive strain and temperature are determined both with thermodynamic analysis and phase-field modeling.

3.2 Specific Methods

3.2.1 Thermodynamic Analysis

The thin-film model used to calculate the free energy of each phase is the same as described in chapter 2.1. Free energy calculations are conducted for compressive strains between 0% and 8%, and for temperatures between 298K and 698K. Additional calculations are conducted for strains between 3% and 5% strain, as this is the experimentally observed region for BFO phase mixtures.

3.2.2 Phase-Field Analysis

For phase-field modeling, methodology described in chapter 2.2 is utilized. Polarizations are randomized between a range of -0.01 to 0.01 for P_x and P_y, and from 0 to 0.01 for P_z to have roughly equal probability for formation of in-plane domain variants, while keeping P_z to be mainly positive to avoid additional complexity of the domain structure. All tests are conducted with "short-circuit" electrical boundary conditions, where the electrical potential on the top and bottom surfaces of each system is set to 0, and is assumed to have fully compensated depolarization fields.

Tests are run for at least 3000 timesteps or until the phase morphology is stable. After data is obtained, the 3D polarization data is counted, and categorized as "*R*" ($[P_x]\sim[P_y]$, $P_z > P_x, P_y$) and "M_C" ($[P_x]\neq[P_y]$, P_x or $P_y \sim 0$, $P_z >> P_x$) phases. The domain walls with transitional polarization values from one phase to the other are not counted as any phase. To differentiate each respective domain from the domain wall regions, only regions with polarizations in a specific range ($P_{z,\,Thermo} - 0.15 < P_{z,\,PhaseField} < P_{z,\,Thermo} + 0.15$) are counted. The total fraction of each phase is determined from the ratio of the counted phases.

3.3 Results and Discussion

3.3.1 –Thermodynamic Analysis

The directional polarization components of each phase can be seen in Figure 3.1. When the compressive substrate strain is in the range of 0.0 ~ -0.03, the equilibrium phase is rhombohedral phase, represented as black dots in Figure 3.1. In this strain range, the out-of-plane polarization component (P_z) increases while the in-plane components of polarization (P_x, P_y) decrease with increasing compressive strain, such that the net polarization ($P = \sqrt[2]{({P_x}^2 + {P_y}^2 + {P_z}^2)}$) remains almost constant around 1.0 C/m^2. When the compressive substrate strain reaches ~ -0.03, there is abrupt enhancement of the net polarization to ~ 1.5 C/m^2, indicating a new stable monoclinic phase. Two variants of the monoclinic phase, M_C and M_A are seen. Although the out-of-plane components of both M_C and M_A are similar and increase with increasing compressive strain, the in-plane components are quite different. For M_A phase (blue dots), the in-plane polarization ($P_x = P_y$) decrease from 0.5 C/m^2 in the rhombohedral phase at this critical strain down to 0.38 C/m^2 in M_A phase. For M_C phase (red dots), one of the in-plane polarization components becomes zero, while the other slightly increases to ~ 0.55 C/m^2. In Fig. 3.1, we assume that Py = 0 in M_C phase. This indicates that under this critical substrate strain, the energy of the rhombohedral phase and

M_C/M_A phases are degenerate. When the compressive substrate strain further increases, the out-of-plane components of M_C/M_A phases further increases while the in-plane components decrease. The net polarization remains almost constant at ~ 1.5 C/m^2 with increasing strain.

The overall Helmholtz free energy densities for *R*, M_C, and M_A phases of the system at room temperature (298K) as a function of compressive strain can be seen in Figure 3.2. As described in Chapter 2.2, the free energy of the system is a function of the polarization of the system, and by extension its strain and temperature through its coupling through electrostriction and the 2nd order Landau coefficient respectively. As a result, changing either external variable can have a profound effect on the free energy and relative stability of BFO's phases. The strain at which the free energy of a given phase is equal to the free energy of the tangent line is referred to as the "critical strain", or the strain where a "pure" phase becomes the most energetically stable form of the system. The increase in energy for the rhombohedral phase correlates well with its decrease in stability with a small increase of strain for both theoretical[6] and experimental results[7]. However, at ~ -0.035 strain, the rhombohedral and monoclinic (M_A and M_C) phases are degenerate. This is lower than the experimentally predicted formation strain (~ -0.043), which may indicate that other factors may limit the formation of the monoclinic phases under a nominal strain, such as domain walls or strain relaxation. M_A and M_C BFO share nearly identical free energy regardless of strain, implying that they are equally likely to form under similar conditions. However, the infinitesimal variation in their critical strains means that it is unlikely that these phases will "de-strain" to decrease their free energy, as such a transition would need to exist in a very small strain range with a prohibitively large energy barrier for the induced energy relaxation.

The phase fractions for the rhombohedral phase obtained from the "lever rule" method for room temperature BFO and upwards can be seen in Figure 3.3. Since the fractions were only

considered between two phases, the variation in phase is linear with respect to strain, indicating that increasing temperature increases the stability of the rhombohedral phase. On the other hand, at fixed temperature, the rhombohedral phase amount decreases with increasing substrate strain, indicating that increasing strain increased the stability of the monoclinic (M_C or M_A) phases. The critical strains of the pure *R* and M_C phases are estimated to be ~ -0.0025 and ~ -0.0674 strain respectively.

The free energy density curves for *R*, M_C, and M_A phases as a function of compressive strain at 498K (200 °C) and 698K (400 °C) can be seen in Figures 3.4 and 3.5, respectively. The critical strains at which the energy densities are equal in *R* phase and M_C/M_A phases are estimated to be ~ -0.04 at 498K and ~ -0.044 at 698K, respectively. The common tangent line connecting the critical strains increases in slope with temperature, indicating that the interval between the critical strains of the *R* and M_C phases increases unevenly. This implies that the rhombohedral phase possesses greater relative stability than the M_C and M_A phases with increasing temperature. In addition, the relative stability of the monoclinic phases shifts as well. The stability region of the M_C phase shrinks as the temperature increases, whereas the M_A phase remains relatively stable at lower strain values in agreement with experimental testing[8]. Figure 3.6 shows the free energy density plots of *R* phase (orange curve) and M_C/M_A phase (blue curve) as a function of polarization at three different combinations of strain and temperature (-3.6% strain at 298K, -0.04 strain at 498K, and -0.044 strain at 698K, respectively.) It is seen that the energy minimum for the two phases in each of these strain/temperature combinations are identical, indicating that the two phases are degenerate. It is also found from Figure 3.6 that the strain required to reach energy degeneracy increases with temperature, correlating with the uneven interval between each phase's critical strains.

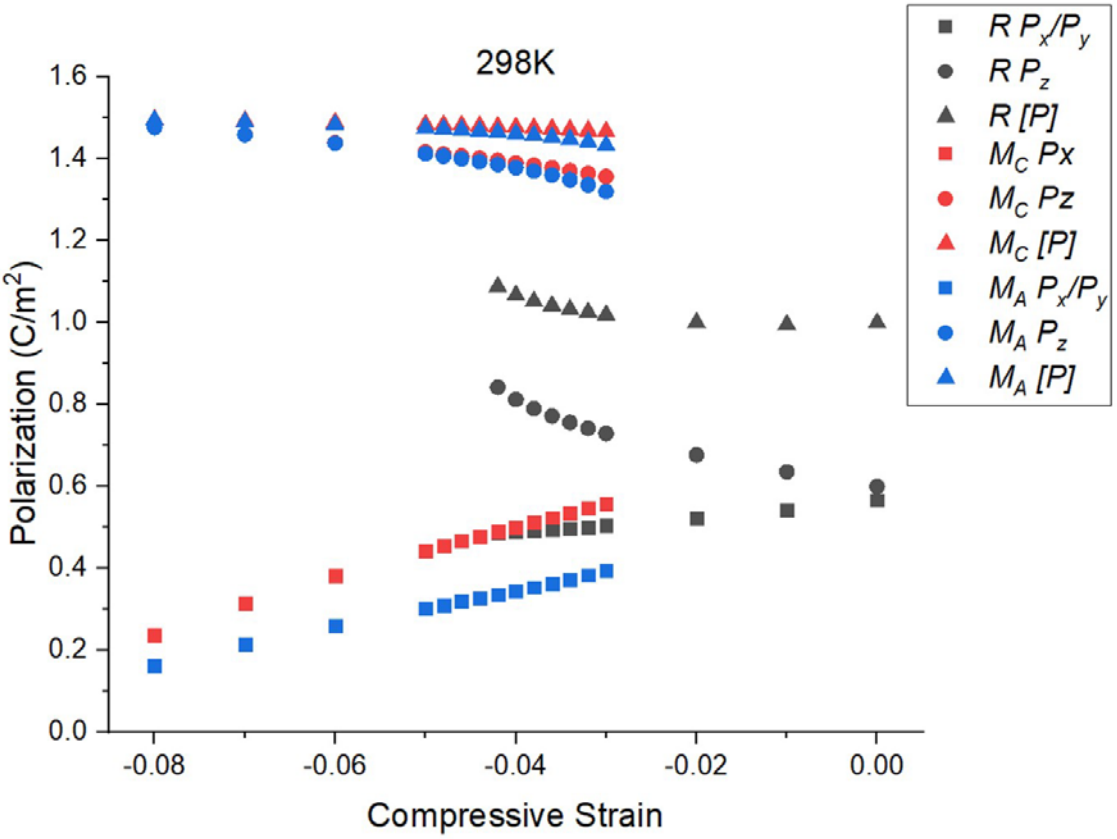

Figure 3. 1: Polarization vs. Compressive Strain at 298K

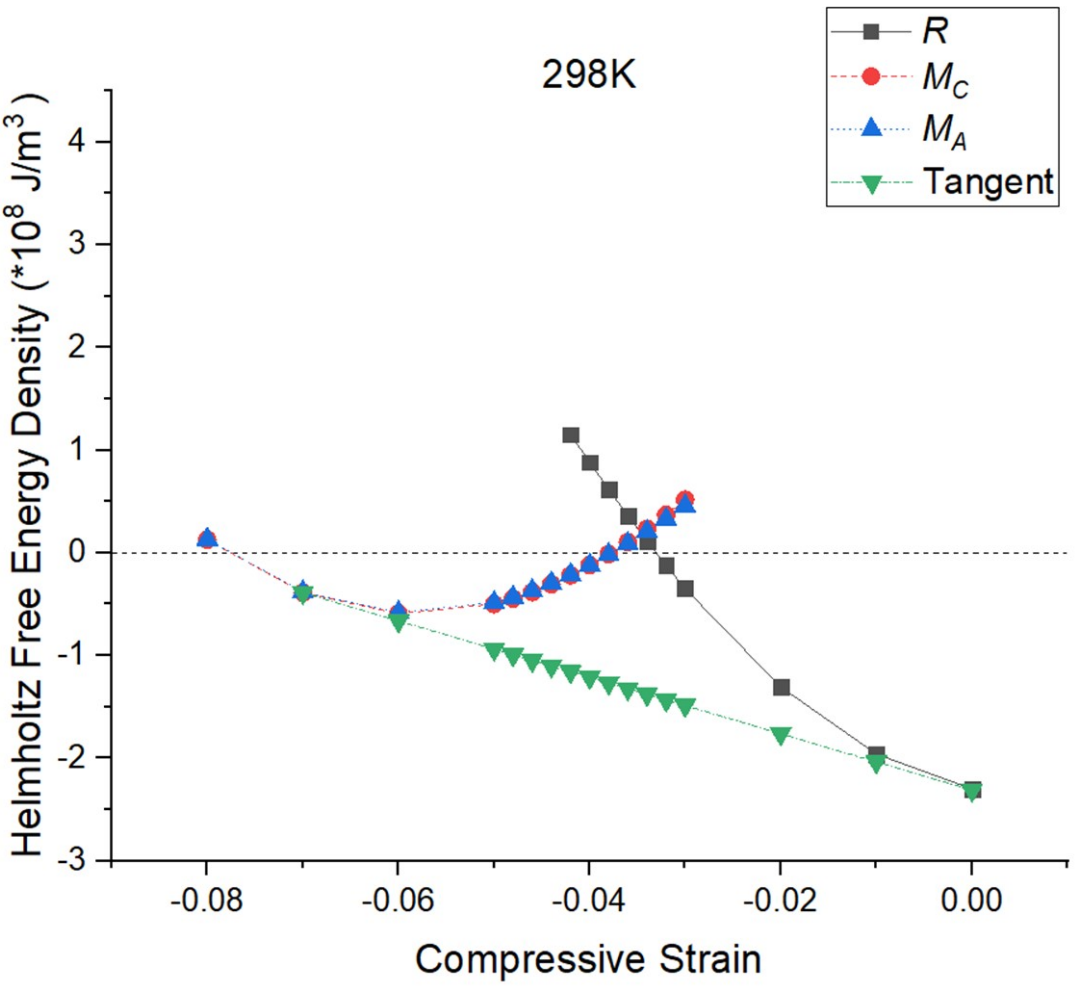

Figure 3. 2: Free energy density vs. Compressive strain at 298K

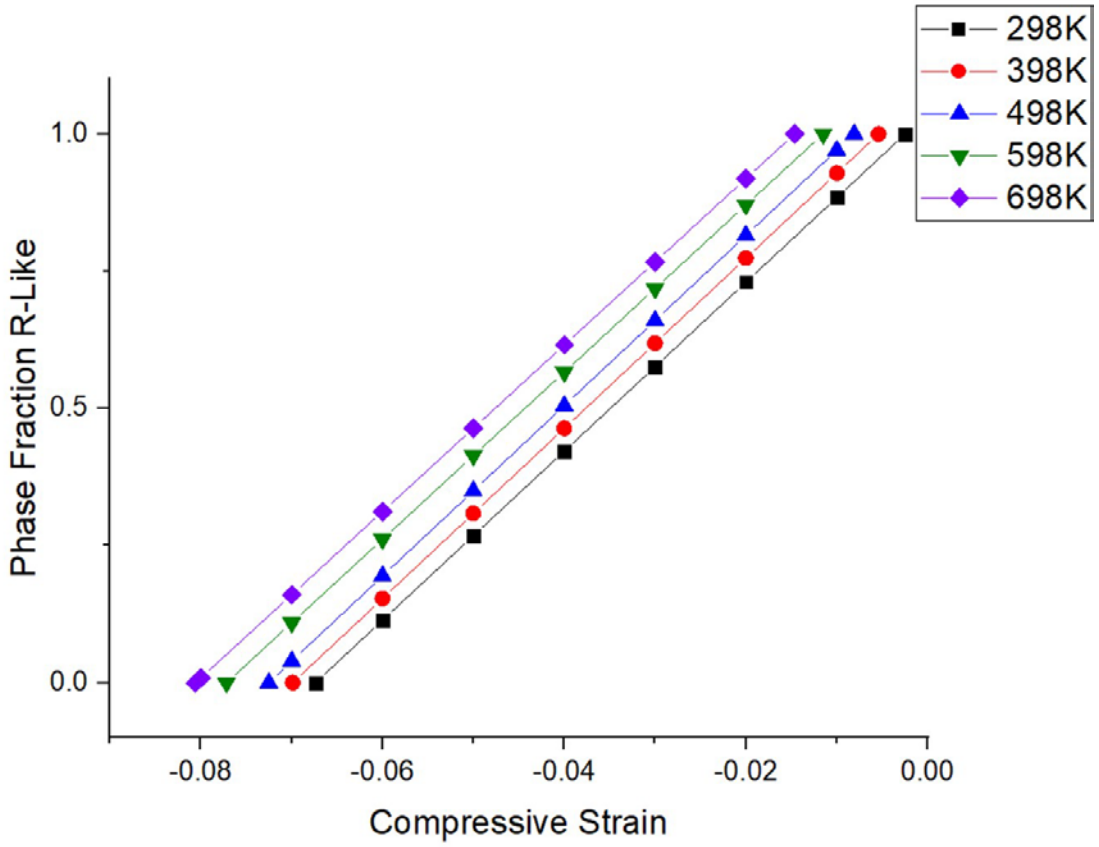

Figure 3. 3: Phase fraction of rhombohedral *BFO vs. Compressive strain from 298K to 698K from Thermodynamic analysis*

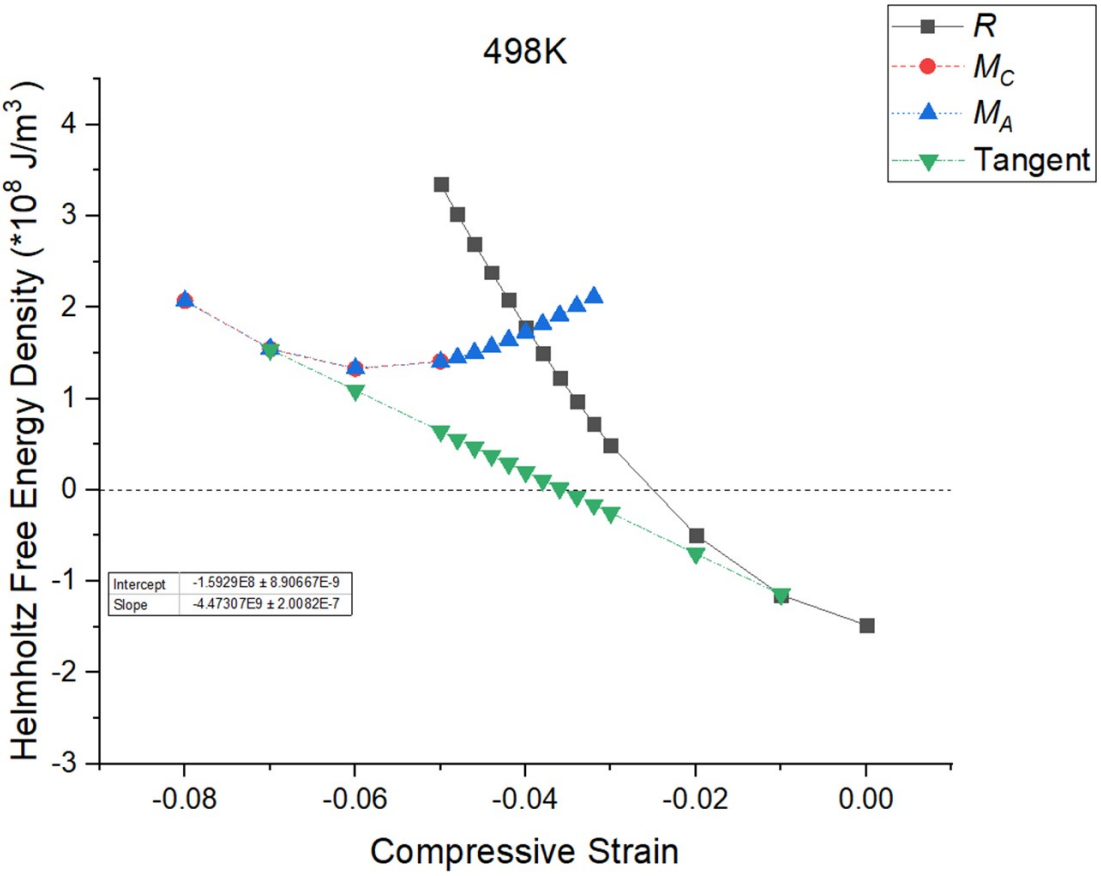

Figure 3. 4: Free energy density vs. Compressive strain at 498K

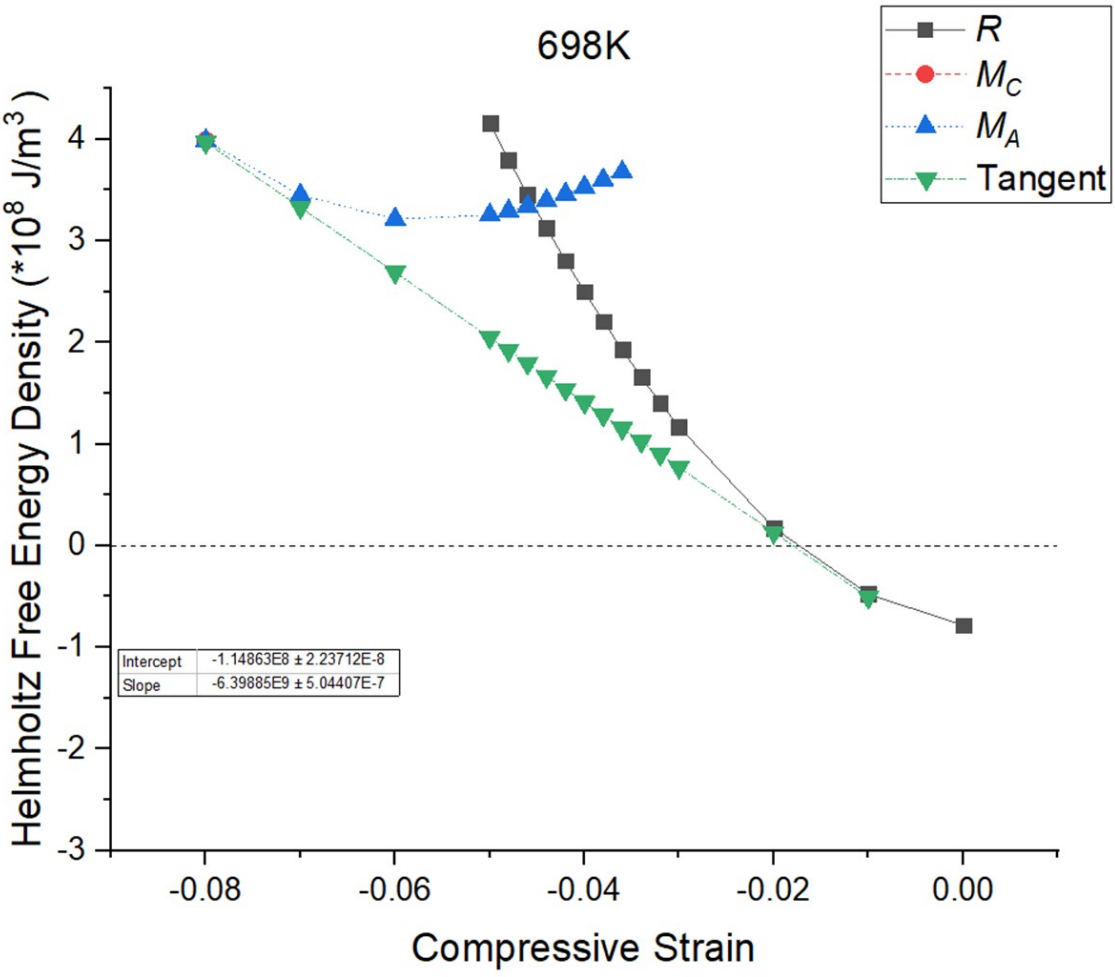

Figure 3. 5: Free energy density vs. Compressive strain at 698K

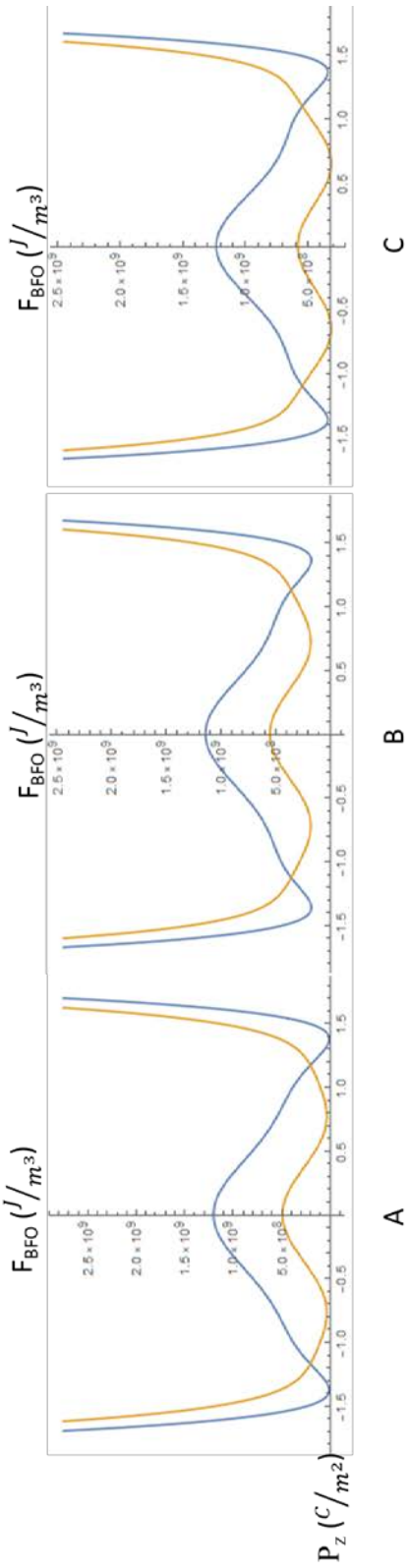

Figure 3. 6: Free Energy Diagram for points of energy degeneracy for BFO's mixed phase regions. Blue and orange lines represent Monoclinic (M_A/M_C) and Rhombohedral BFO free energy density respectively, (A) 298K: 3.6% Compressive Strain (B) 498K: 4.0% Compressive Strain (C) 698: 4.4% Compressive Strain

3.3.2 Phase-Field Analysis

Thermodynamic analysis cannot fully account for spatial effects of strain and domain formation. Thus, phase-field modeling emerges as an important tool for analysis of ferroelectric thin films. The phase-field model describes the system as distinct ferroelectric domains with consistent properties (Polarization, Strain, etc.) across each domain. Thus, the properties of each domain as well as their distribution can be observed across the entire structure. The domain structures obtained from the phase-field modeling at room temperature and under compressive strains from 0%, 4%, and 7% can be seen in Figure 3.7. At 0% strain, the structure is composed of BFO rhombohedral domain variants. Since P_z's initial values are set to be randomly distributed from 0 to 0.01, only four out of the eight rhombohedral domain variants (with $P_z>0$)) are seen. As strain is increased to 4%, mixed *R* and M_C phases of BFO are stable, in agreement with prior theoretical results[9]. At 7% strain, the equilibrium domain structure is composed of pure M_C and the domain walls form 45° angles to mediate alternating in-plane polarizations.Unlike the thermodynamic model, the highly polarized M_A phase does not appear, despite having similar free energy to the M_C phase. Since this phase could possess a greater polarization gradient across its symmetric domains, its domain wall energy would be much larger than the M_C phase, which may explain why the phase-field system favors M_C BFO.

The equilibrium domain structures at 498K and 698K can be seen in Figures 3.8 and 3.9, respectively. Increasing the temperature by 200K does not appreciably change the domain structure under 0% and 7% strains, but the bands of M_C BFO begin to shrink at 4% strain. Increasing the temperature by another 200K fully removes the M_C BFO from the 4% strain structure. At 698K, the alternating bands of M_C BFO at 7% strain increase in size, possibly an

effect of the growing metastability of the M_C phase not just relative to rhombohedral BFO, but relative to the paraelectric phase.

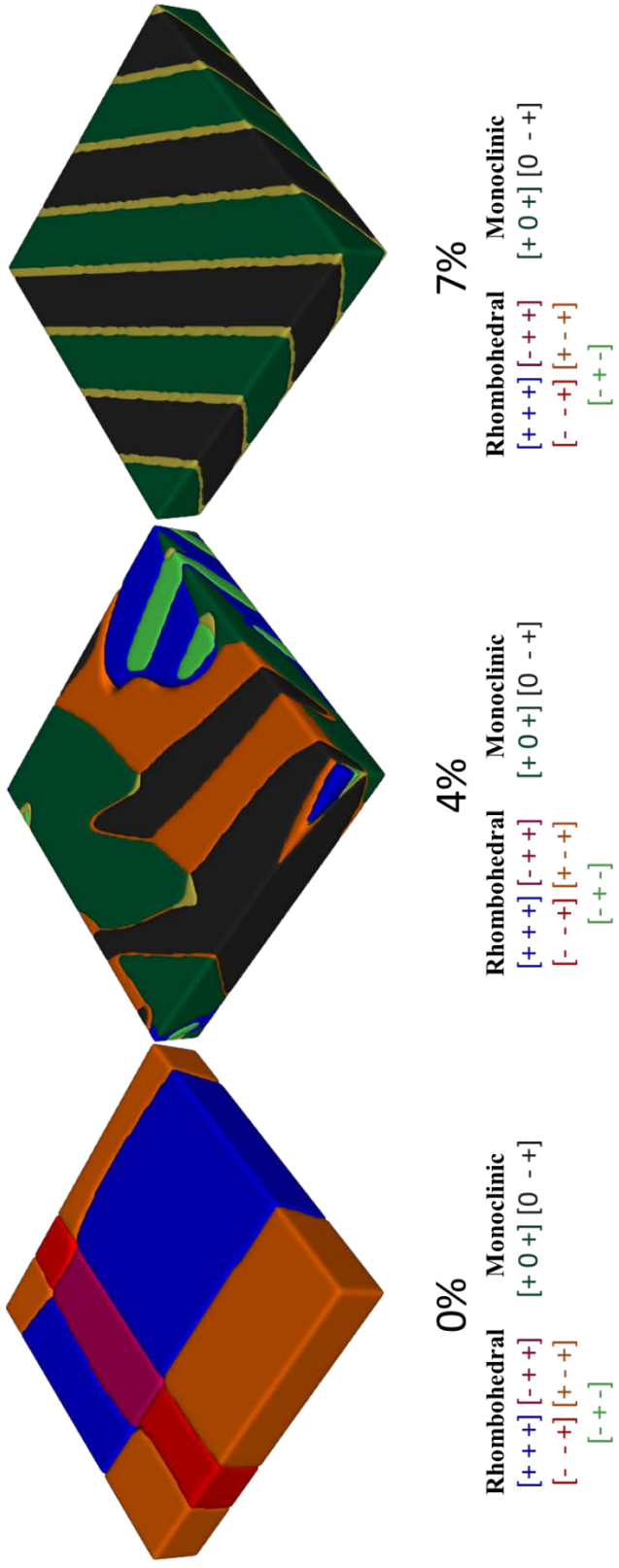

Figure 3. 7: Phase-field simulation of BFO domain structure at 298K under 0%, 4%, and 7% strains

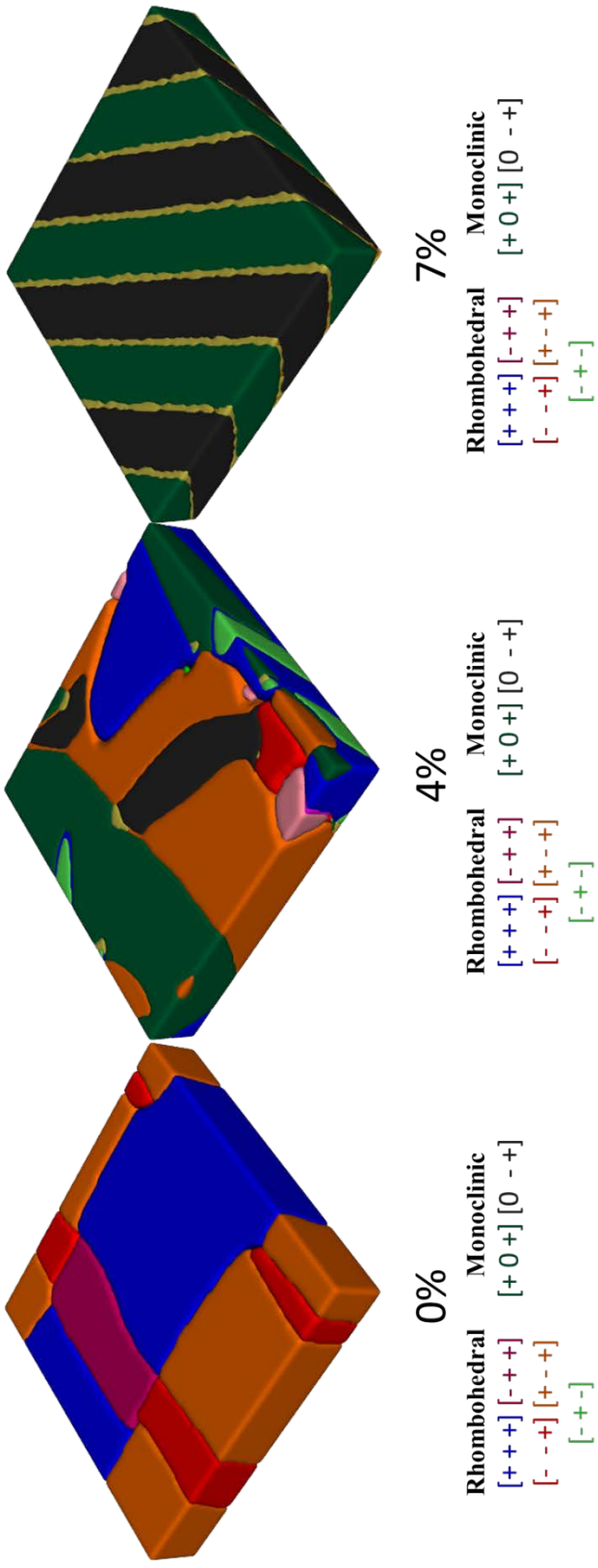

Figure 3. 8:Phase-field simulation of BFO domain structure at 498K under 0%, 4%, and 7% Strains

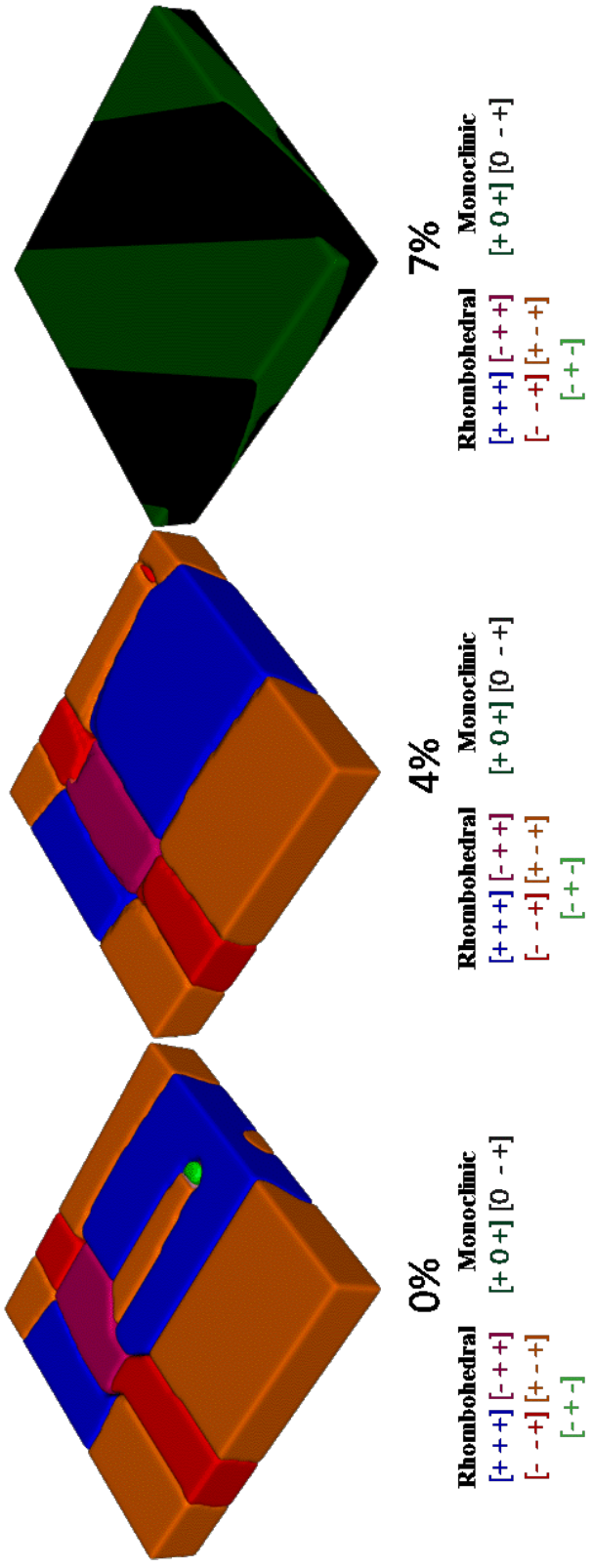

Figure 3. 9: Phase-field simulation of BFO domain structure at 698K under 0%, 4%, and 7% strains

The phase fraction of rhombohedral BFO as a function of compressive strain calculated from phase-field simulation is summarized in Figure 3.10. Compared to the thermodynamic analysis, the phase-mixture region is much narrower, likely due to the effects of domain wall energy. Under low compressive strain (0.0 ~ -0.02), *R* phase is dominant in the domain structure, and the emergence of new M_C phase enhances the gradient (domain wall) energy, which is strongly unfavored. Therefore the threshold strain for stable R/M_C mixed phase becomes larger than from thermodynamic analysis. Similarly, under large compressive strain, M_C phase becomes stable which inhibit the formation of *R* phase due to gradient energy "penalty", resulting in a smaller critical strain where M_C phase transforms into R/M_C mixed phase. Therefore the strain window of mixed R/M_C phase from phase-field simulation is much narrower than that predicted from thermodynamic analysis. When temperature increases, the threshold strain where R/M_C mixed phase emerge becomes also larger, indicating that *R* phase is more stable at higher temperature. This agrees with our previous thermodynamic analysis.

Based on the results in Figures 3.3 and 3.10, a compressive strain/temperature diagram of the *R* and M_C critical strains is plotted in Figure 3.11, with the thermodynamic model's critical strains represented as lines, and the phase-field model's strains represented as individual points. Due to the effects of domain wall energy the mixed-phase region of the phase-field model is much narrower than the thermodynamic model. Phase-field simulation also indicated that the strain window for R/M_C mixture decrease with increasing temperature. Nevertheless, both models show good agreement on the effects of strain and temperature on the relative stability of the rhombohedral and monoclinic phases and behavior of their phase boundaries.

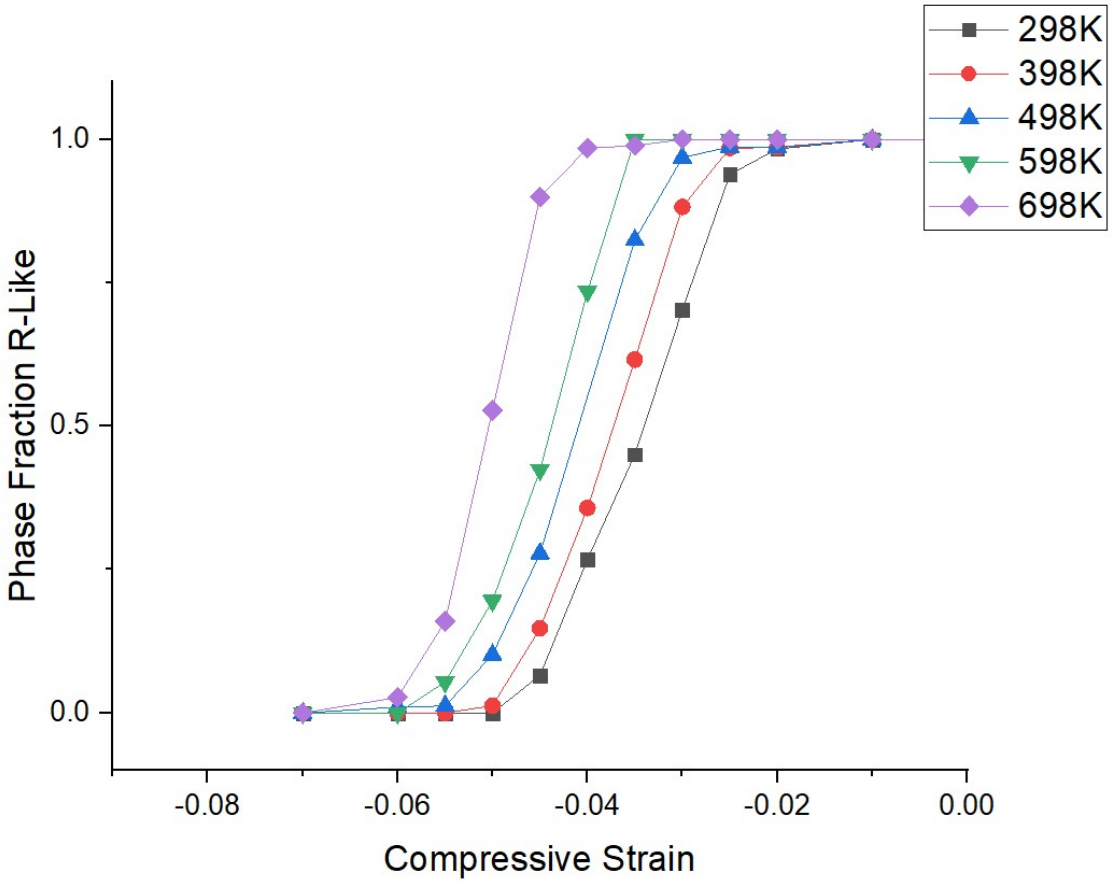

Figure 3. 10: Phase fraction of R-like BFO with substrate strainfrom Phase-field model

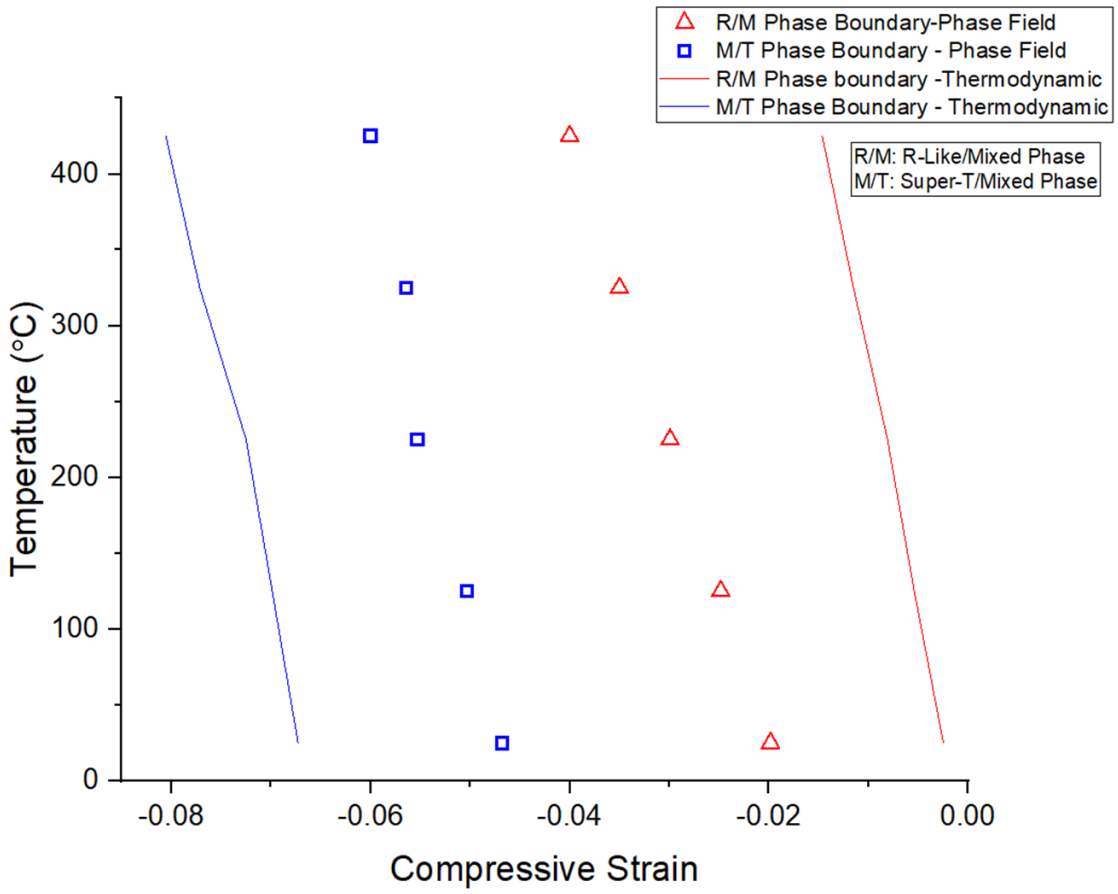

Figure 3. 11: Compressive Strain/Temperature Diagram of BFO's critical strains. Solid lines indicate thermodynamic calculations, and scattered symbols indicate phase-field simulation results.

References

[1] Siemons, W. *et al.* A complete strain–temperature phase diagram for $BiFeO_3$ films on $SrTiO_3$ and $LaAlO_3$ (0 0 1) substrates. *J. Phys. D. Appl. Phys.* **47,** 034011 (2014).

[2] Wang, J. *et al.* Epitaxial $BiFeO_3$ multiferroic thin film heterostructures. *Science (80-.).* **299,** 1719–1722 (2003).

[3] Ederer, C. & Spaldin, N. A. Effect of epitaxial strain on the spontaneous polarization of thin film ferroelectrics. *Phys. Rev. Lett.* **95,** 2–5 (2005).

[4] Zeches, R. J. *et al.* A Strain-Driven Morphotropic Phase Boundary in $BiFeO_3$. *Science (80-.).* **326,** 977–980 (2009).

[5] Beekman, C. *et al.* Phase Transitions, Phase Coexistence, and Piezoelectric Switching Behavior in Highly Strained $BiFeO_3$ Films. *Adv. Mater.* **25,** 5561–5567 (2013).

[6] Infante, I. C. *et al.* Bridging multiferroic phase transitions by epitaxial strain in BiFeO3. *Phys. Rev. Lett.* **105,** 057601 (2010).

[7] Sando, D. *et al.* Control of ferroelectricity and magnetism in multi-ferroic BiFeO3 by epitaxial strain. *Philos. Trans. R. Soc. A Math. Phys. Eng. Sci.* **372,** 20120438–20120438 (2014).

[8] Liu, H.-J. *et al.* Structural study in highly compressed BiFeO 3 epitaxial thin films on YAlO 3. *J. Appl. Phys.* **112,** 052002 (2012).

[9] Xue, F., Li, Y., Gu, Y., Zhang, J. & Chen, L.-Q. Strain phase separation: Formation of ferroelastic domain structures. *Phys. Rev. B* **94,** 220101 (2016).

Chapter 4: Results – Electrical Switching (Analytical and Phase-Field)

4.1 Introduction

The myriad domains of BFO complicate its electrical switching behavior, as changes in a domain via electrical energy induce changes in the domain wall energy and elastic energy as well. Depending on the orientation of the thin film, the possible domains to be switched can vary[1 2], and multiple domain orientations can interfere with one another[3]. In addition, increasing temperature can even remove ferroelectric switching of phases entirely[4]. However, these properties can be used for the control of multiferroic properties, such as ferroelectric control of magnetism[1] and selective creation of domain walls[5]. As a result, understanding the effects of strain and temperature on domain formation and stabilization is vital to controlling these domains and the interplay between their unique electromechanical properties.

4.2 Specific Methods

4.2.1 Thermodynamic Analysis

The thermodynamic model is the same as described in Chapter 2, with the addition of the electrostatic component, as seen in (2.10). The electrical field is oriented perpendicular to the film surface, i.e., along [001] direction. For thermodynamic analysis, the electric field applied to the system is homogeneous.

Electrical switching tests were conducted at 0%, 4%, and 6% compressive strains, representing strains that favor rhombohedral BFO, "mixed" BFO, and M_A/M_C BFO respectively. Temperature is varied from 298K to 698K in 200K increments. The electrical field is increased in increments of 10^8 V/m until the "coercive field" is achieved for all phases, or until a prohibitively large electric field is achieved. Since the thermodynamic system is "dimensionless" and cannot distinguish individual domain switching, it instead determines the relative free energy and stability

of the domains with positive ("un-switched") and negative ("switched") polarizations. If a domain is no longer stable under the given conditions, the phase is considered "switched".

4.2.2 Phase-Field Model

Initial polarization values for P_x and P_y are randomized between a range of 0 to 0.01 for both *R* and M_A/M_C electrical switching, and the initial polarization values for P_z are randomized between 0 to 0.01 for *R* switching and 1.5 to 1.51 for M_A/M_C switching. All initial polarization values are kept positive to minimize the effect of domain interactions that are not induced by the coercive field.

A homogeneous electrical field is applied to the surface of the system increment is applied to the system every 100 steps. A hysteresis loop is generated by increasing this electrical field until the system undergoes electrical switching, and then decreasing the electrical field until the reversed electrical switching is achieved as well. Tests are conducted for *R* switching for compressive strains 2% and under, and for M_C or M_A switching for compressive strains from 3% to 6%.

4.3 Results and Discussion

4.3.1 Thermodynamic Analysis

The results of electrical switching at room temperature for 0%, 4%, and 6% compressive strain under room temperature (298K) are plotted in Figures 4.1, 4.2, and 4.3, respectively. After a certain electrical field threshold, the positive-oriented domains disappear, leaving only the negative domains. The field at which this occurs can be considered to be the phase's "coercive field". The coercive field is the electrical field required to induce a domain's transformation to a symmetrically related domain with polarization inverted along the direction of the applied electrical field. The thermodynamic results indicate that the coercive field for rhombohedral BFO is ~4.5 ($*10^8$ V/m) under 0% substrate strain, ~2.5 and ~5.5 ($*10^8$ V/m) for M_C and M_A BFO

respectively at 4% strain, ~6.5 and ~13.5 (*10^8 V/m) for M_C and M_A BFO respectively at 6% strain. The small coercive field for M_C BFO may be a result of a switching "pathway", or a phase transformation occurring before a domain transition as a response to electrical bias. Several experimental results have indicated that M_C BFO can convert to R BFO[7 8] or R/M_C mixed phase BFO under the influence of an electrical tip bias[9 10]. Since the effects of interacting domains cannot be approximated by this thermodynamic model, the cause of the low coercive field is likely due to the metastability of the M_C phase. The polarization magnitude of the M_A and M_C phases of BFO are similar, but the coercive field of M_A BFO is drastically higher than its counterpart. The monoclinic tilt of M_C BFO has been theorized to aid in its low coercive field[11]. However, both M_A and M_C BFO possess monoclinic distortions. If this is the case, what determines the "stubbornness" of the M_A phase? The thermodynamic stability data from Chapter 3 suggest that M_A BFO is stable over a much wider range of strains than M_C BFO as temperature increases. The polar stability of this phase may impede its ability to undergo electrical switching, and thus diminish its ferroelectric properties.

The polarization values and coercive fields of the phases of BFO at 498K at 0%, 4% and 6% compressive strain can be seen in Figures 4.4, 4.5 and 4.6 respectively. Compared to 298K, the "coercive field" for all ferroelectric phases decreases. At 4% strain, the R and M_C phases are not stable enough to model electrical switching in the thermodynamic model. The stability and "coercive field" of M_C BFO at 6% Strain is highly reduced in particular, from ~6.5 (*10^8 V/m) to ~2.5 (*10^8 V/m). This may be a result of the decreased stability of the phase with increasing temperature. Increasing the temperature to 698K continues to decrease the stability of the R and M_A phases and causes the M_C phase to disappear entirely, as seen in Figures 4.7, 4.8 and 4.9. The stability of a phase under a thin film's thermal and mechanical boundary conditions may correlate

well with its sensitivity to electrostatic inputs. As a result, tuning the electronic inputs to a system as a function of its thermal and mechanical constraints may be vital to designing ferroelectric materials for electronic applications.

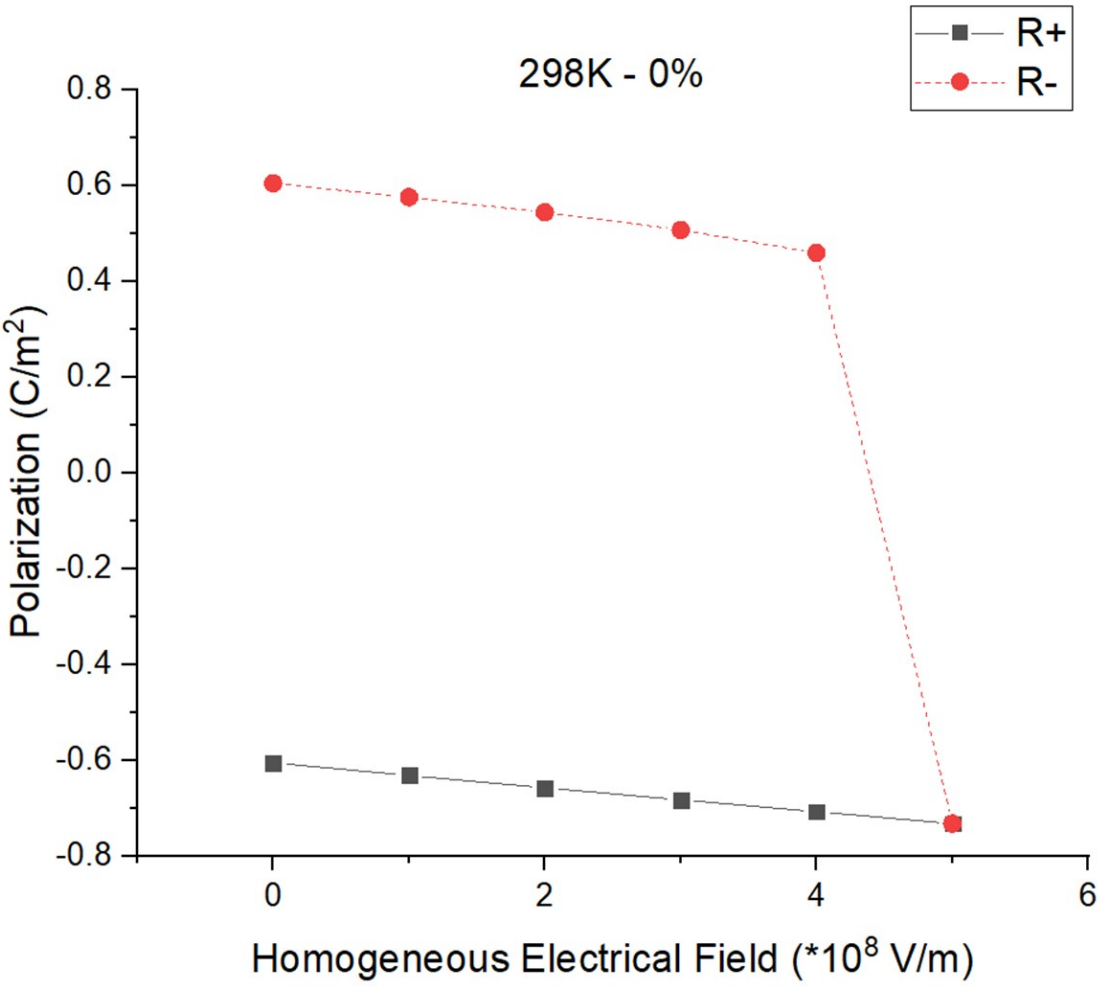

Figure 4. 1: Electrical switching behavior of R-like BFO at 298K and 0% compressive strain.

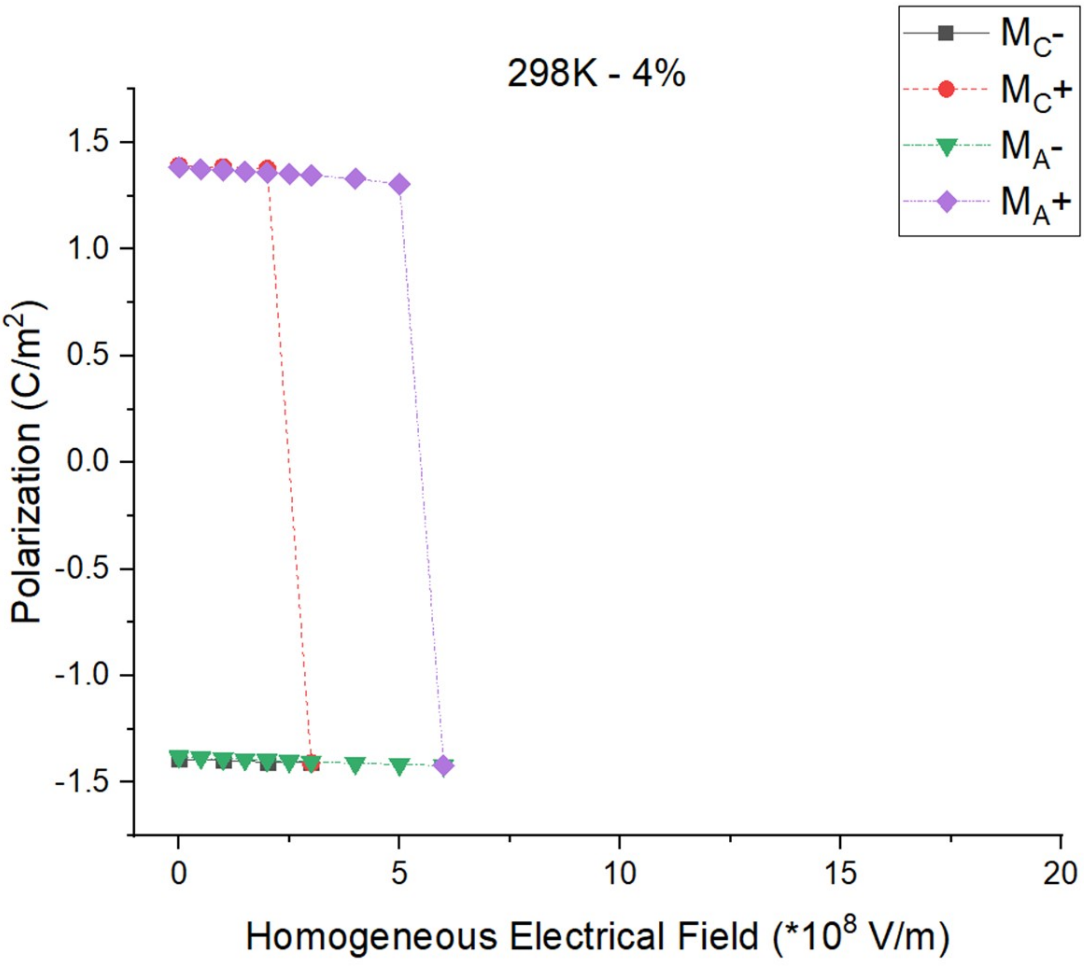

Figure 4. 2: Electrical switching behavior of M_C/M_A-like BFO at 298K and 4% compressive strain

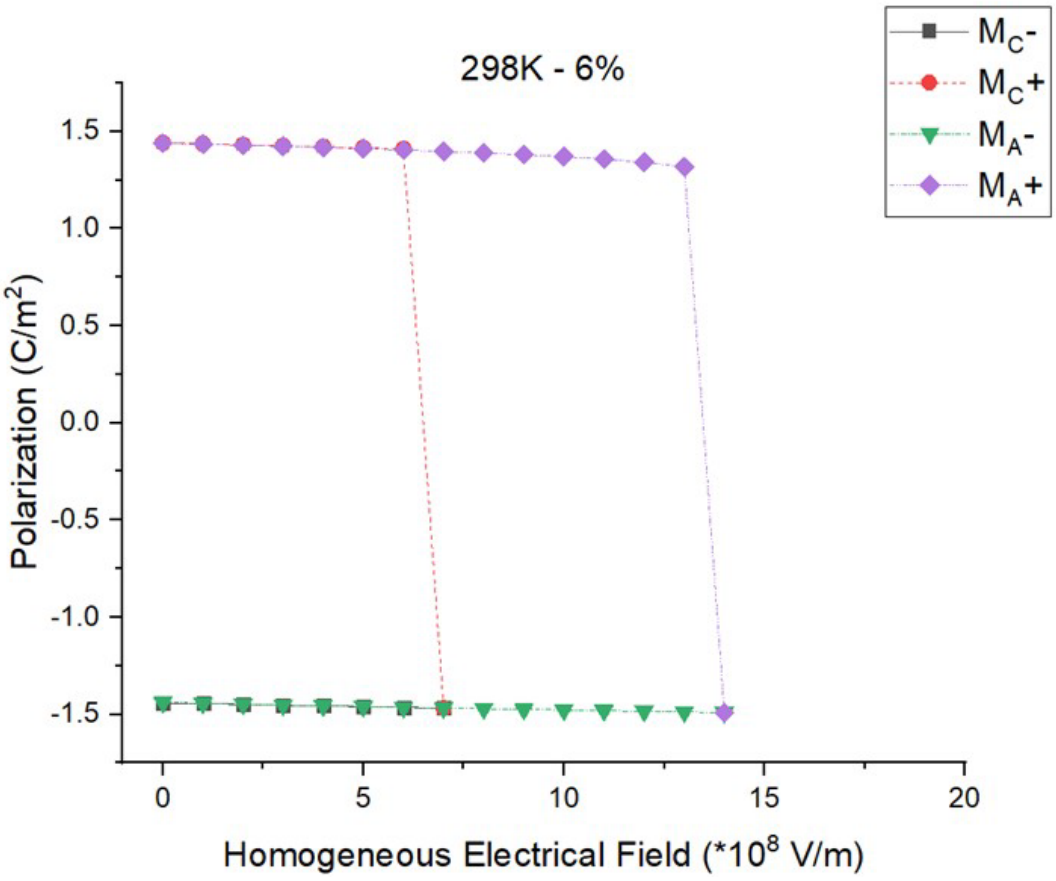

Figure 4. 3: Electrical switching behavior of M_C/M_A-like BFO at 298K and 6% compressive strain

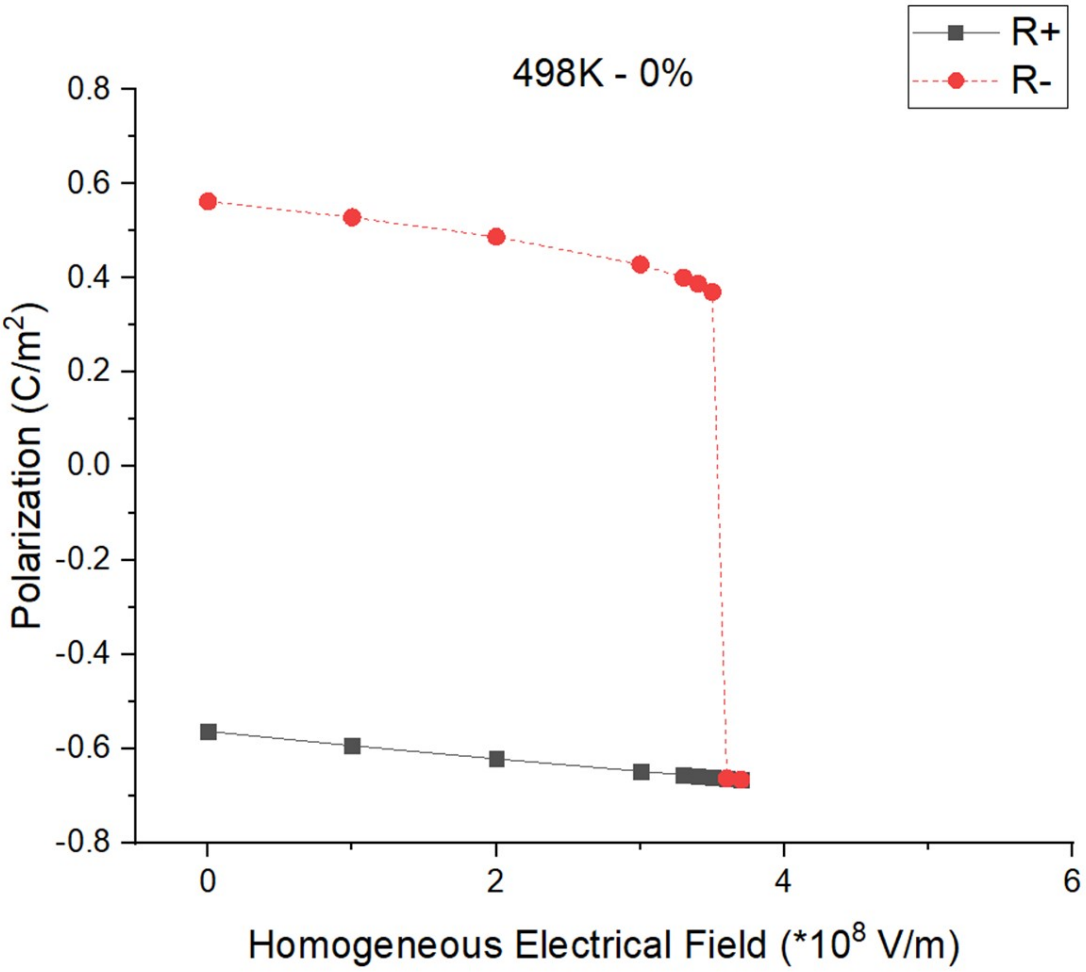

Figure 4. 4: Electrical switching behavior of R-like BFO at 498K and 0% compressive strain

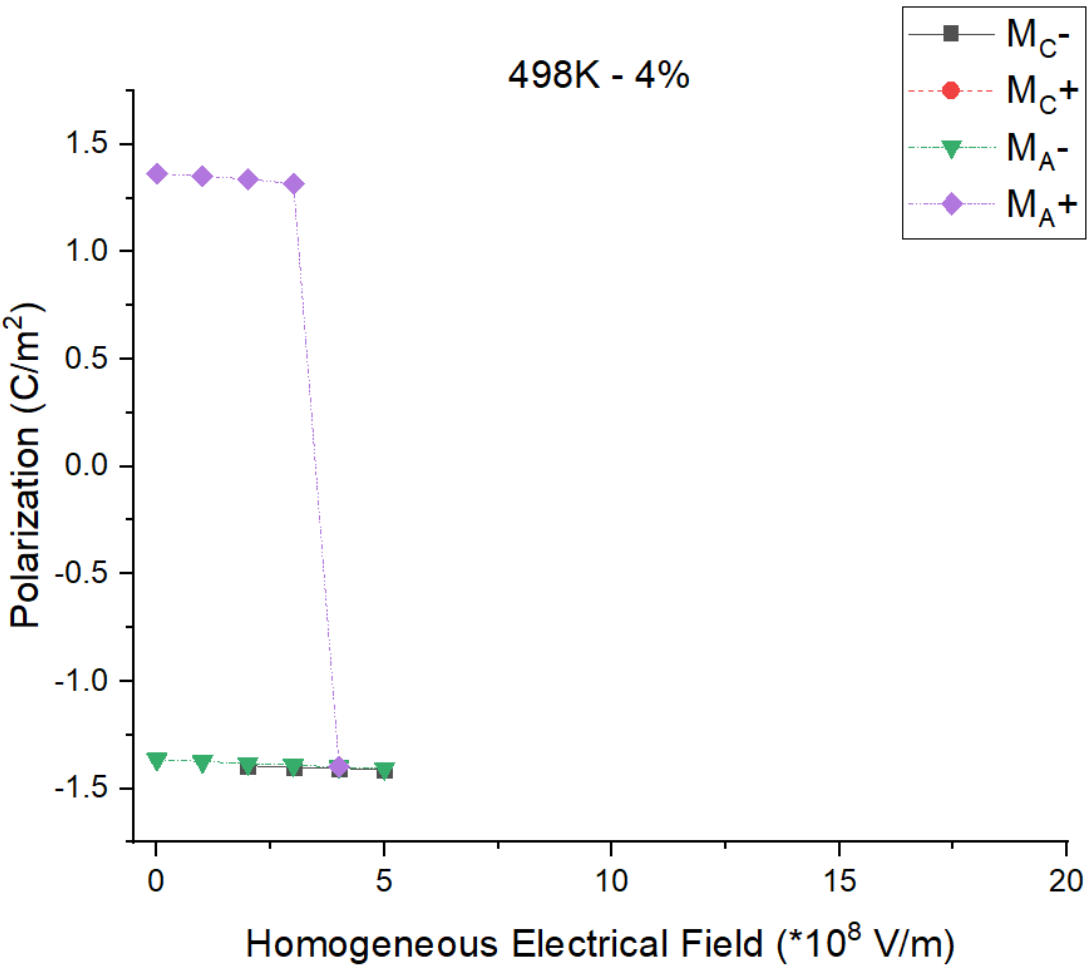

Figure 4. 5: Electrical switching behavior of M_C/M_A-like BFO at 498K and 4% compressive strain

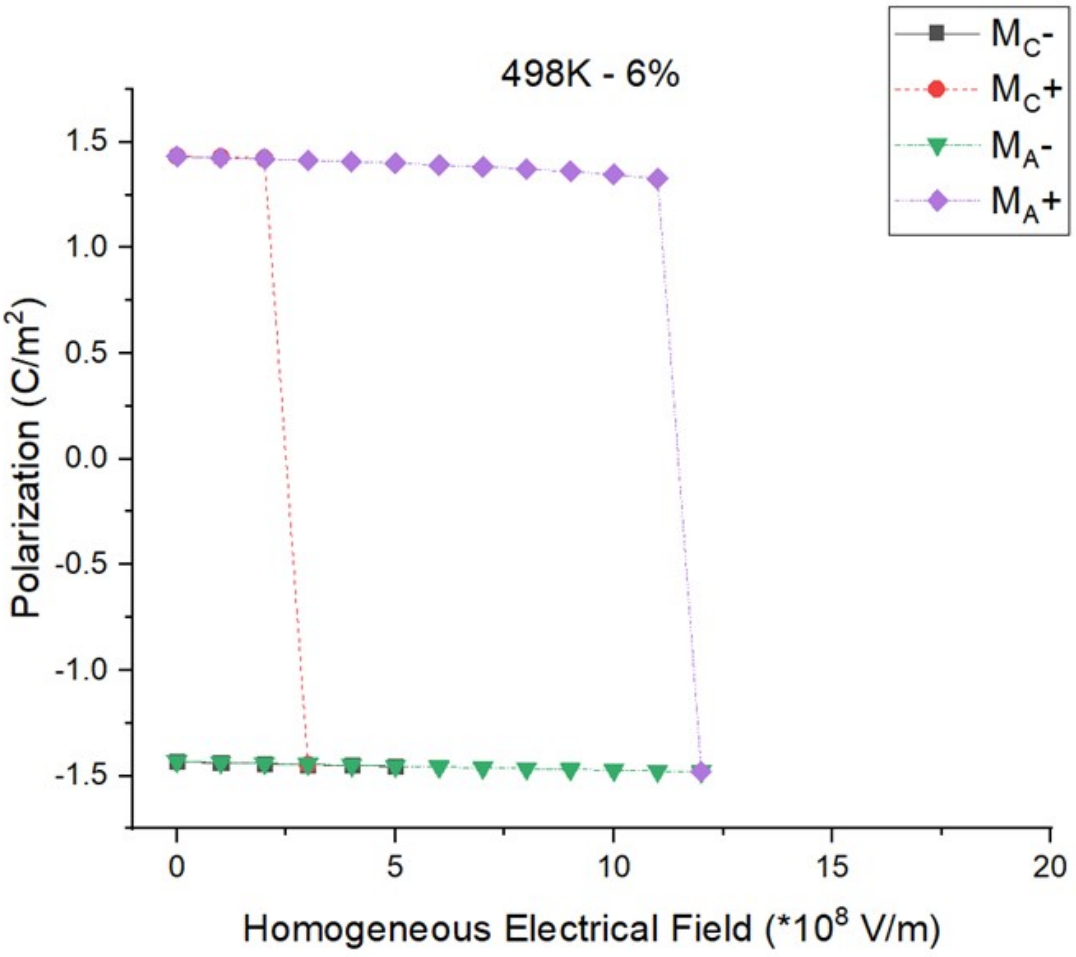

Figure 4. 6: Electrical switching behavior of M_C/M_A-like BFO at 498K and 6% compressive strain

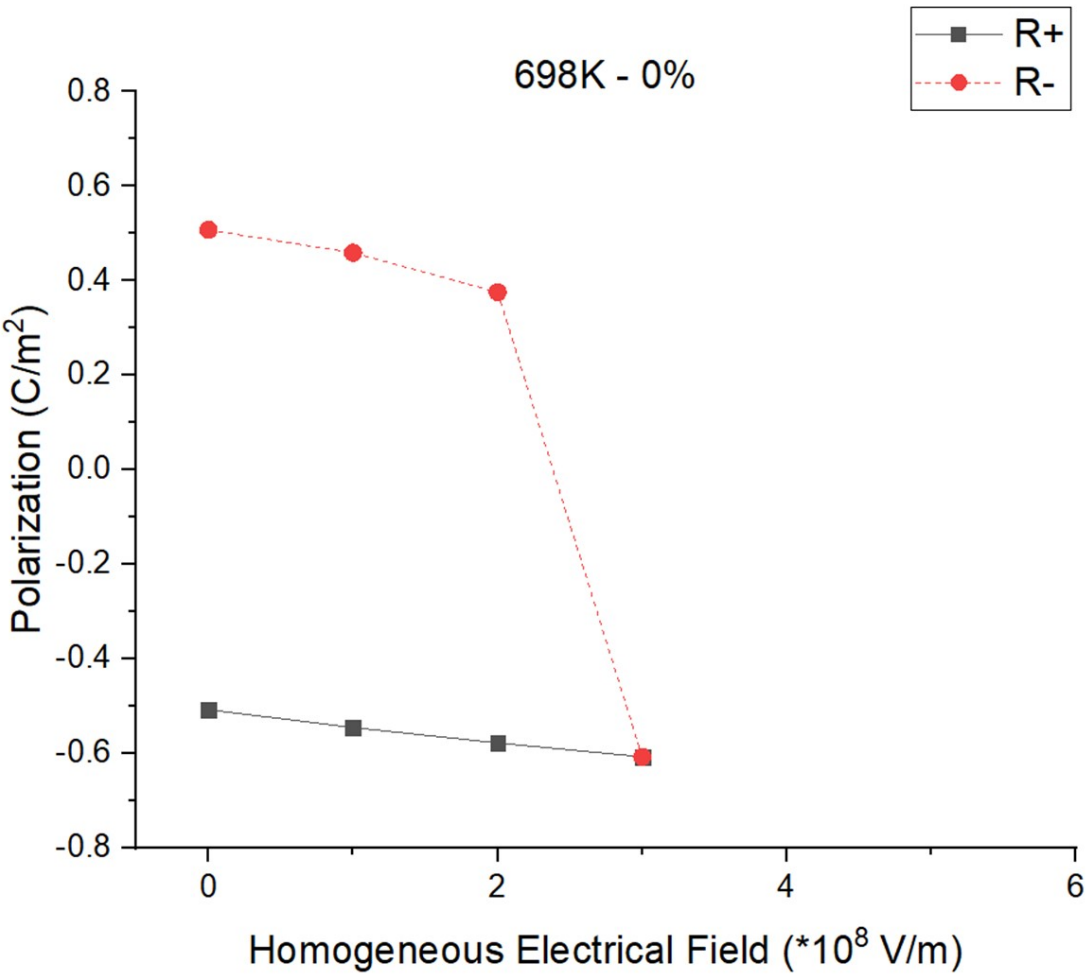

Figure 4. 7: Electrical switching behavior of R-like BFO at 698K and 0% compressive strain

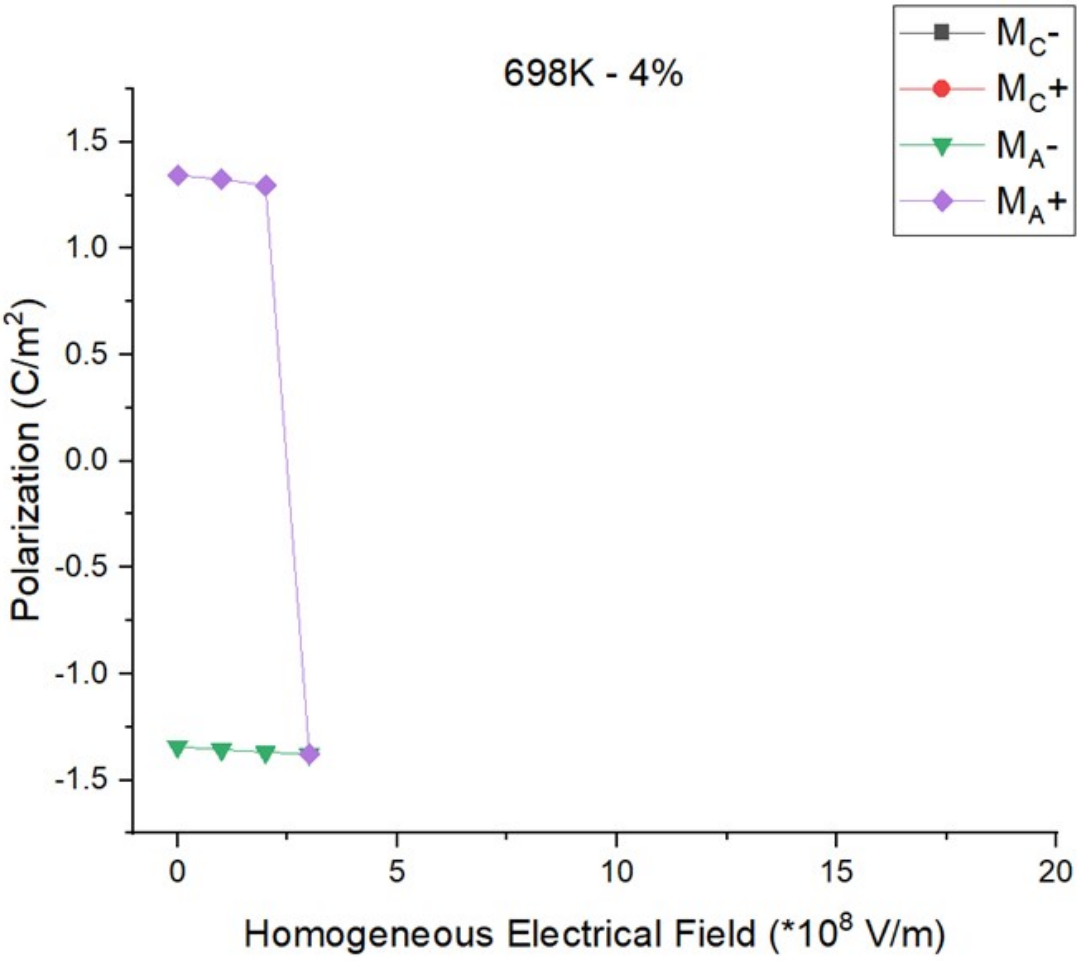

Figure 4. 8: Electrical switching behavior of M_C/M_A-like BFO at 698K and 4% compressive strain

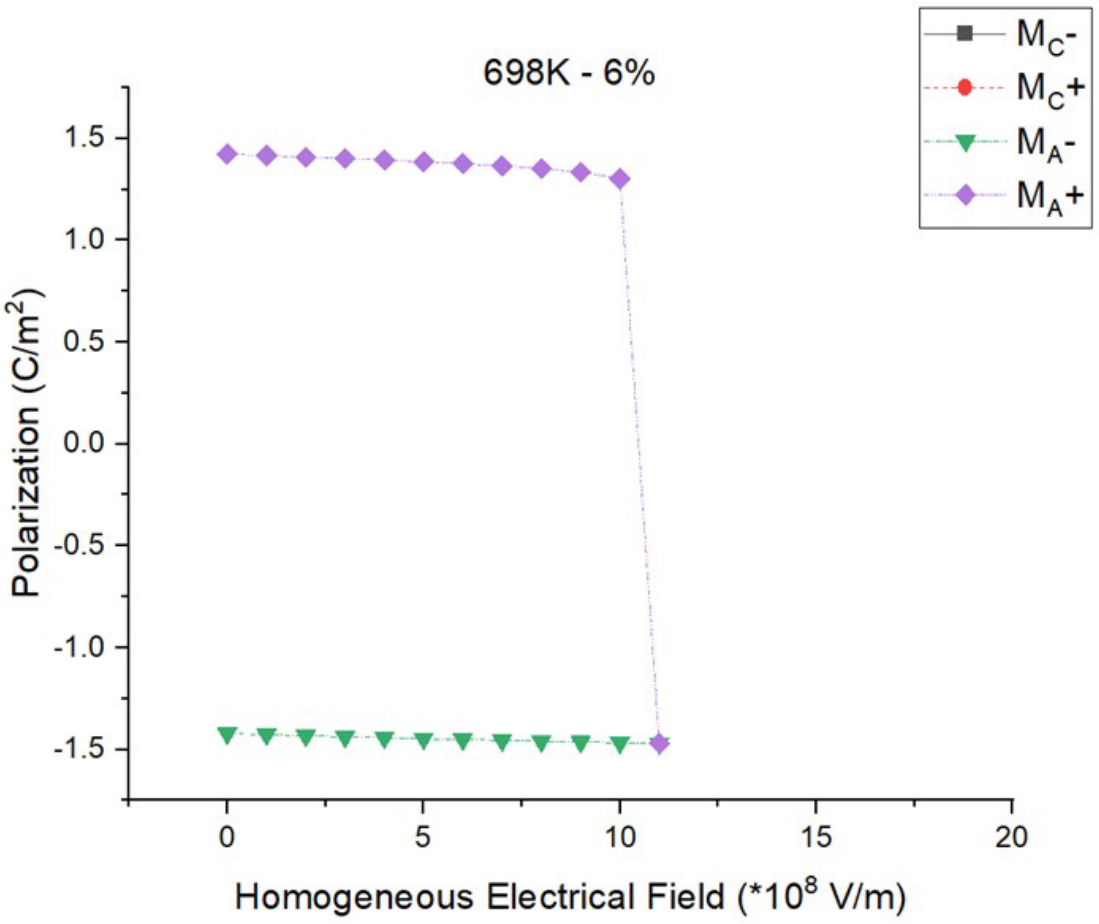

Figure 4. 9: Electrical switching behavior of M_C/M_A-like BFO at 698K and 6% compressive strain

4.3.2 Phase-field model

Since phase formation pathways play a pivotal role in the electrical switching behavior of BFO, phase-field modeling is utilized to model the progression of BFO's phases as a function of increasing electrical bias. The hysteresis behavior of BFO at room temperature without strain can be seen in Figure 4.10. Under these conditions, the system undergoes a single rhombohedral domain switch ($[P_x\ P_y\ P_z]$: $[+\ +\ +] \rightarrow [+\ +\ -]$). However, the magnitude of the phase-field model's coercive field is slightly larger than the thermodynamic model's. This may be explained by additional switching boundaries induced by the effects of domain formation and ferroelastic strain, as the switching domains have structural mismatch[2].

The hysteresis loop at 4% compressive strain can be seen in Figure 4.11. The increase in strain induces the formation of the alternating M_C phase. Introducing the electrical field to the system induces the formation of the rhombohedral phase at the boundaries between the alternating M_C domains in agreement with prior theoretical and experimental results[9] [10] and eventually undergoing electrical switching to a single inverted M_C domain. The system retains similar behavior on its reversed hysteresis. However, formation of single *R* phase BFO was found in the reverse hysteresis pathway, as well as single phase M_A BFO. This may imply that both of these phases are stable over very small regions of applied electrical bias. The transition from high to low polarization phases as bias is applied to the system may imply that the relative free energy of these phases plays a part in their electrical switching behavior. Since BFO can reduce its free energy by "de-straining" into distinct phases, the relative shift in free energy of these phases may define the electrical switching/transformation behavior of this and other ferroelectric materials. In addition, since the electrical switching takes place within a single axis of polarization, the system undergoes

a ferroelastic shift as well, creating an additional energy term that can be relaxed via phase de-strain. The momentary shift to M_A may relate to the similarity in free energies between it and the M_C phase[12], and the difference in the gradient energies between them. Figure 4.12 displays the hysteresis loop at 6% compressive strain. While the formation of R/M_C bands still occur, their stability with respect to the electric field is greatly diminished. In addition, the region over which electrical switching occurs is much narrower. As the system is highly strained, the M_C phase is relatively stable compared to the R phase, and thus does not possess the small region of stability for that phase to remain stable.

The hysteresis loops at 0% strain from 298K-698K are compared in Figure 4.13. The hysteresis behavior at 0% strain follow similar trends as temperature increases, but the coercive field required to induce electrical switching decreases, in agreement with the prior results of thermodynamic analysis. Increasing the strain to 4% reveals similar trends with increasing temperatures, as seen in Figure 4.14. However, the relative change in stability with respect to temperature of the M_C and R phases appears to slightly shift the regions of mixed phase stability. At 698K, another transition from pure R to mixed M_C/R phase appears, resulting in a more gradual transition from R to M_C BFO. The results of increasing temperature at 6% strain are shown in Figure 4.15. The coercive field continues to decrease with increasing temperature. However, unlike the systems at 4% strain, the increased stability of the R phase does not induce an additional transformation into an additional stable phase region in the hysteresis loop as temperature increases.

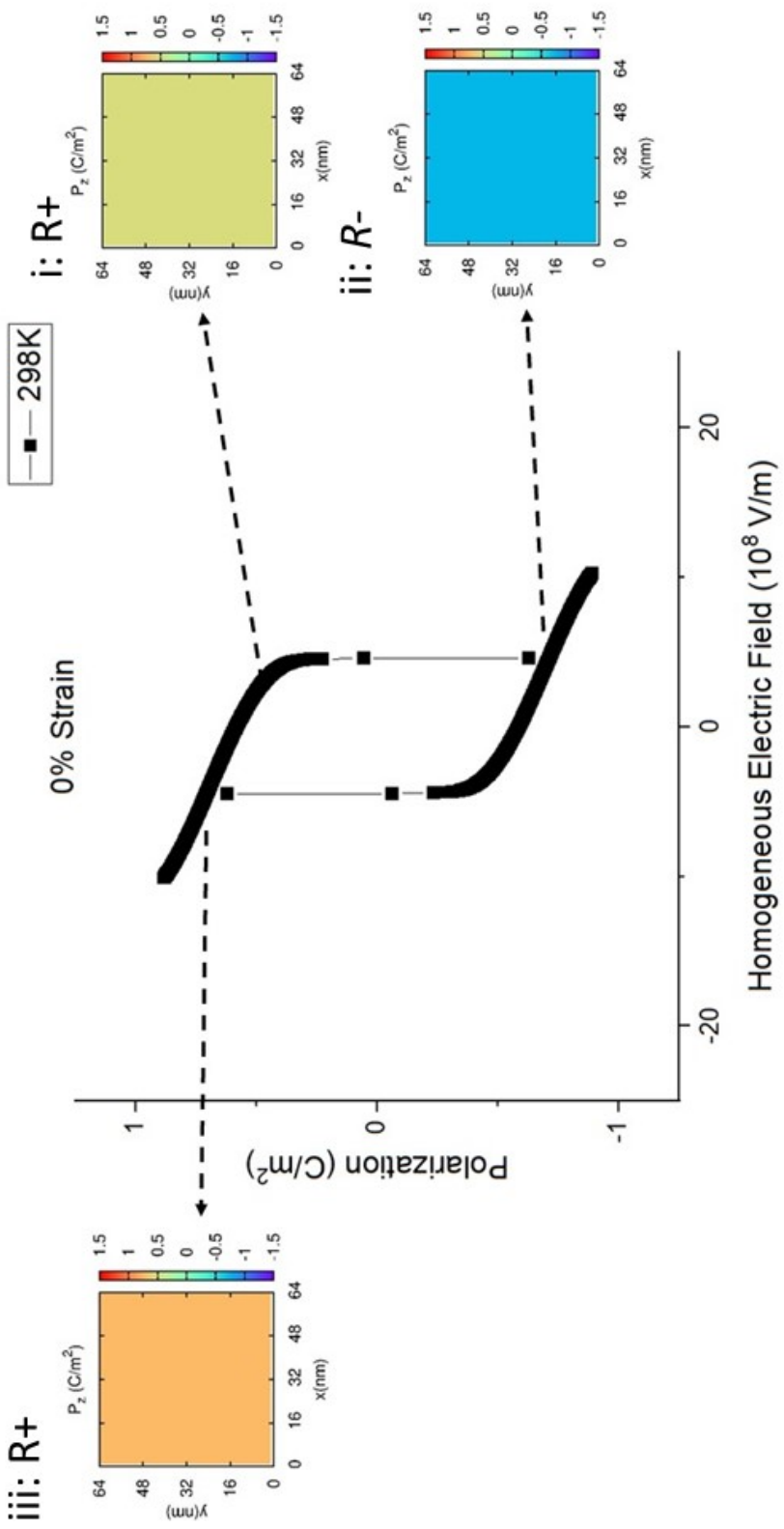

Figure 4. 10: BFO electrical hysteresis behavior at 0% Strain and 298K

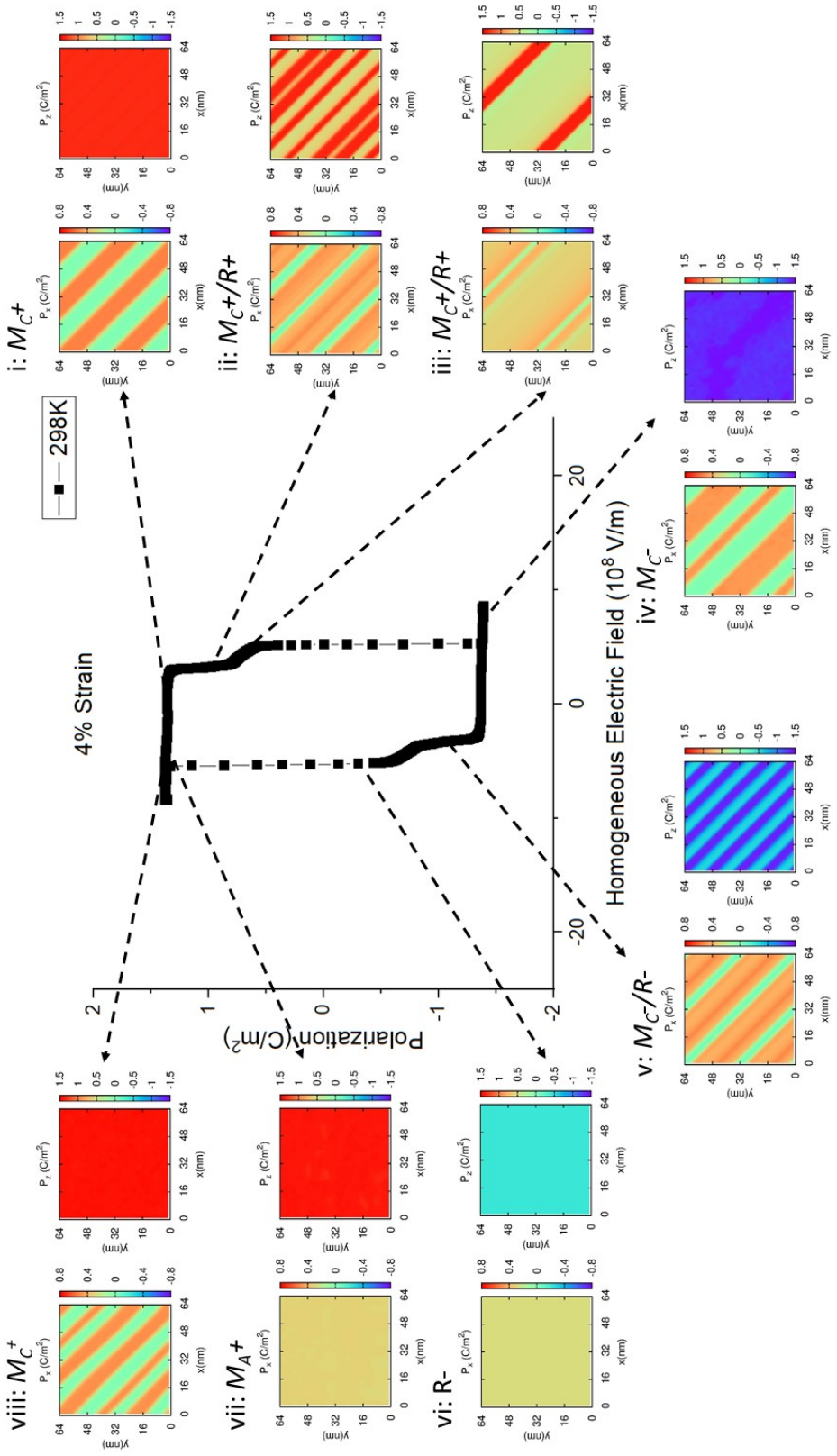

Figure 4. 11: BFO electrical hysteresis behavior at 0% Strain and 298K

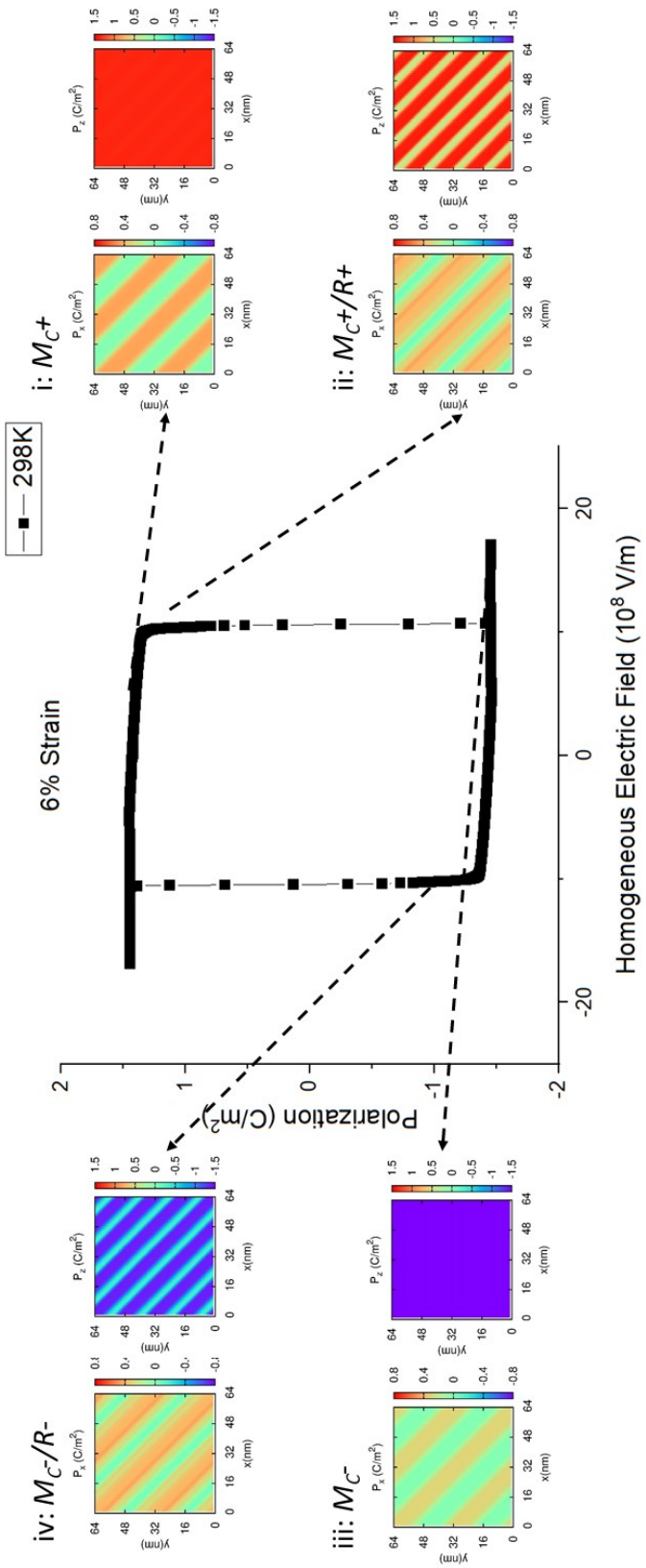

Figure 4. 12: BFO electrical hysteresis behavior at 6% Strain and 298K

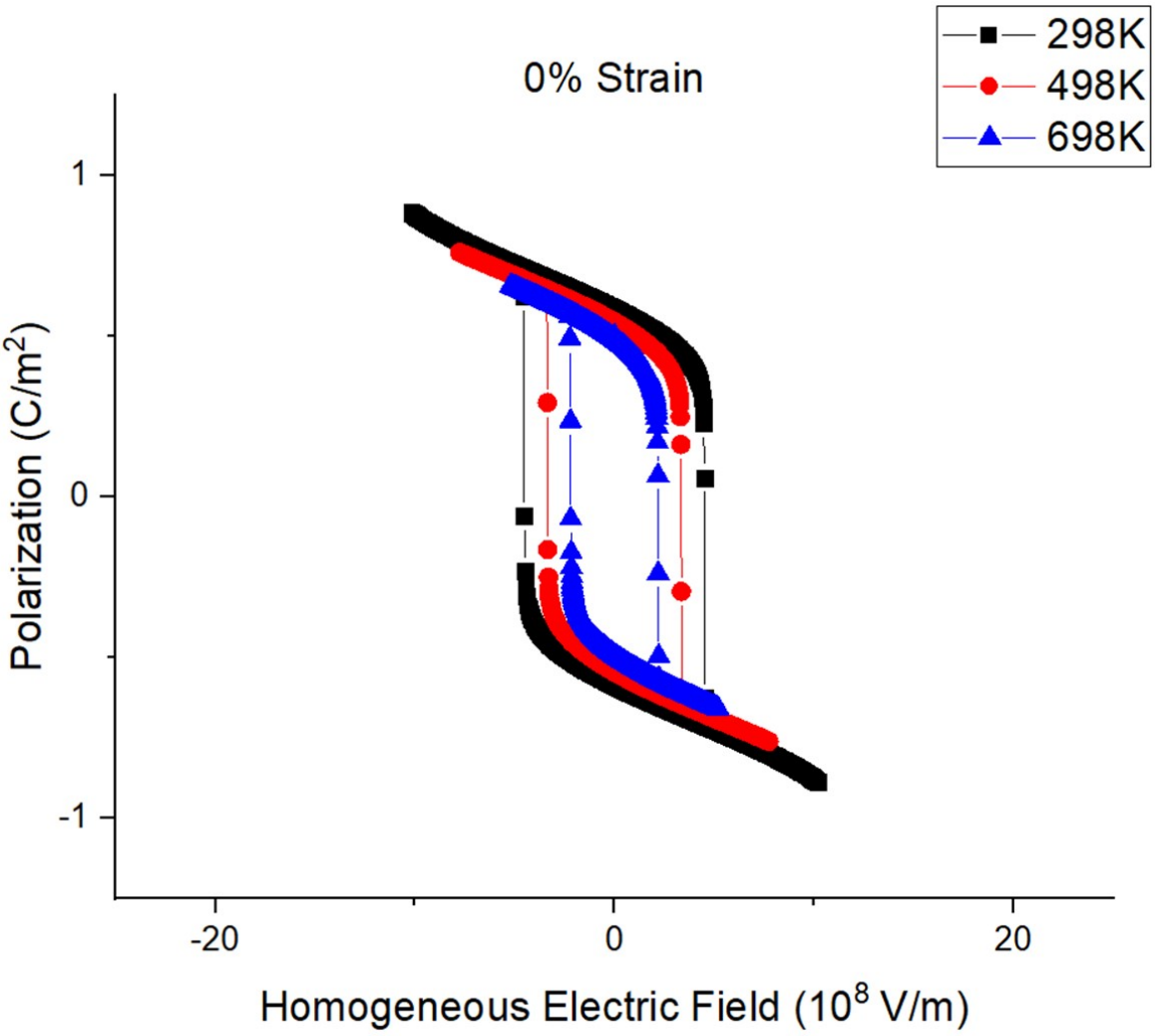

Figure 4. 13: BFO electrical hysteresis behavior at 0% Strain from 298K-698K

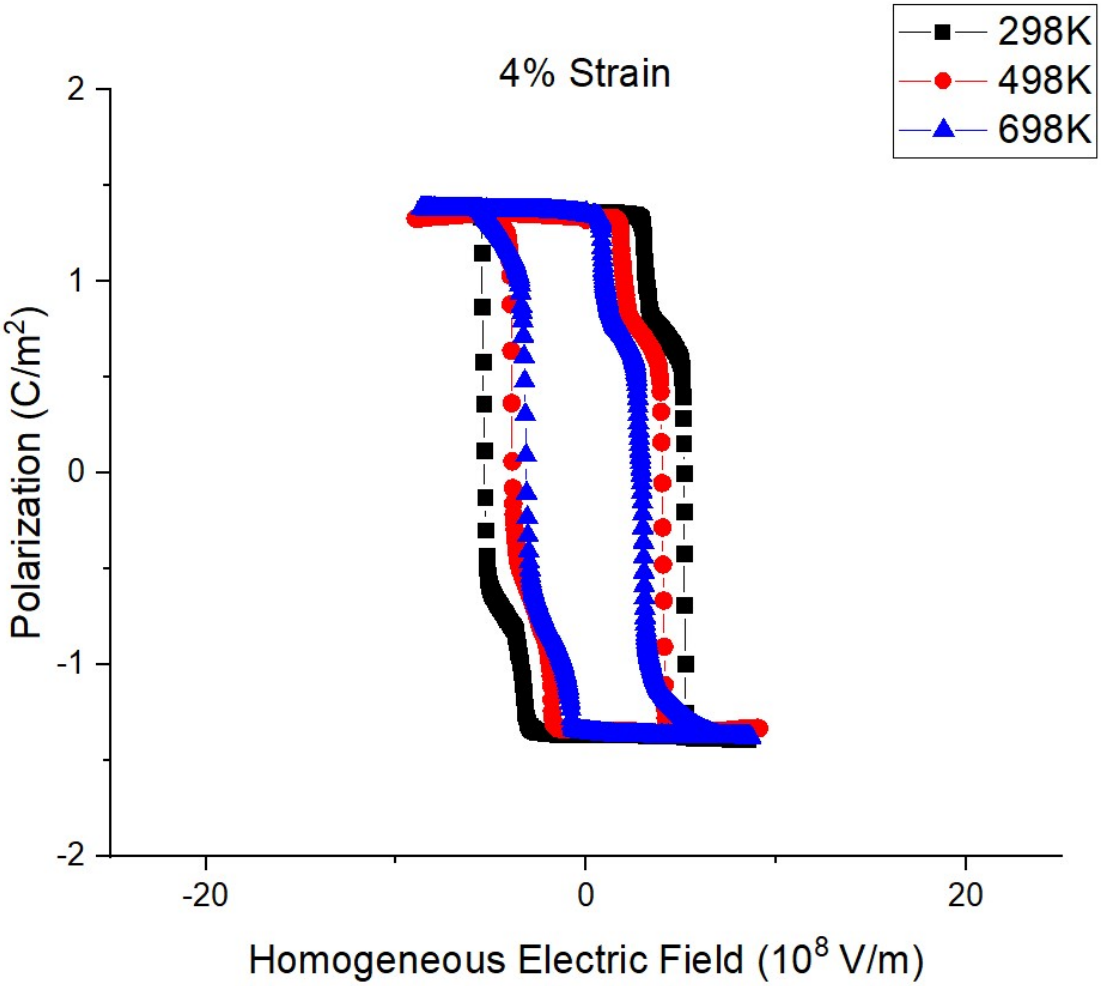

Figure 4. 14: BFO electrical hysteresis behavior at 4% Strain from 298K-698K

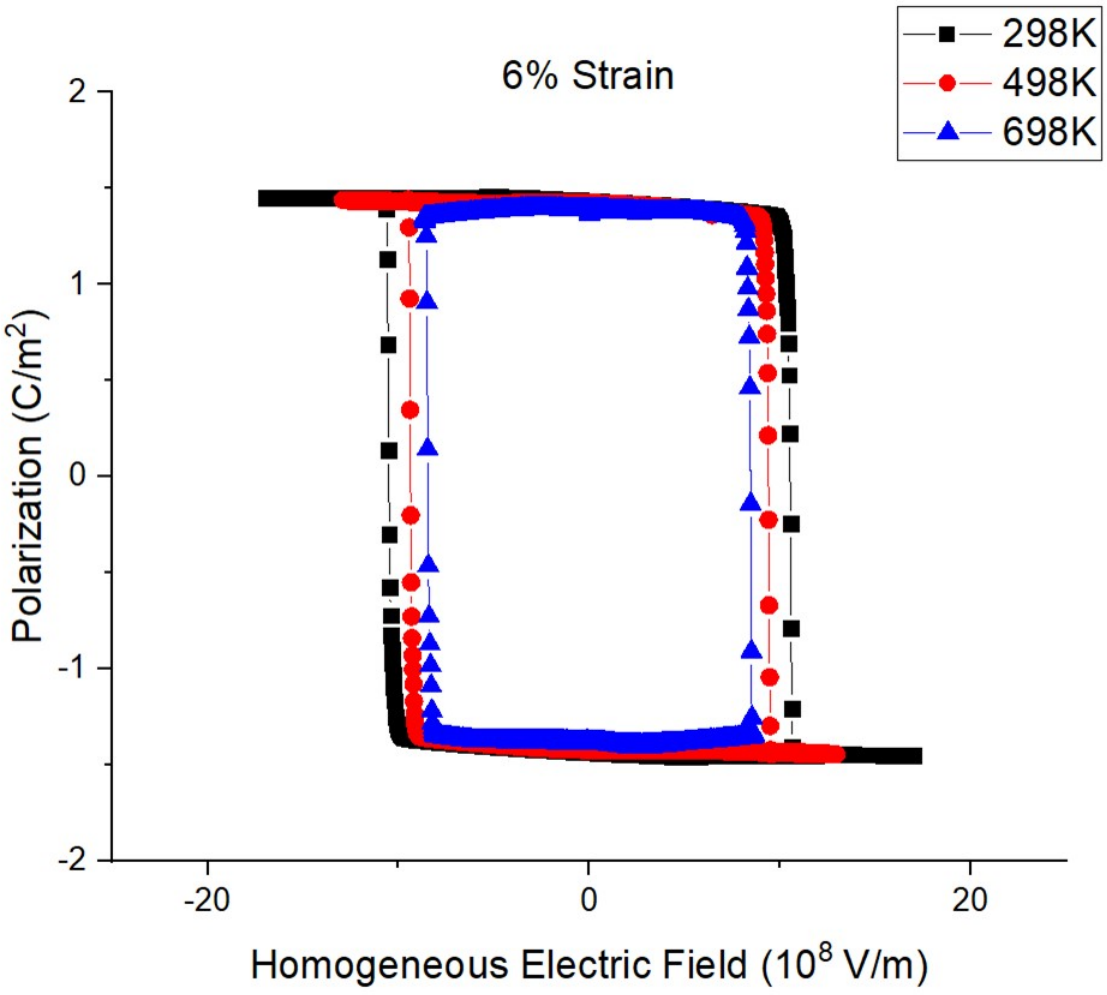

Figure 4. 15: BFO electrical hysteresis behavior at 6% Strain from 298K-698K

4.3.3 Thermodynamic – Phase-Field Comparison

*Table 4. 1: Coercive Field" (*10^8 V/m) of BFO phases from thermodynamic analysis. X indicates that all domain variants were thermodynamically unstable.*

	E_C - 298K	E_C - 498K	E_C - 698K
R - 0%	~4.5	~3.5	~2.5
M_C - 4%	~2.5	X	X
M_C - 6%	~6.5	~2.5	X
M_A - 4%	~5.5	~3.5	~2.5
M_A - 6%	~13.5	~11.5	~10.5

*Table 4. 2: Coercive Field" (*10^8 V/m) of BFO phases from phase-field simulation.*

	E_C - 298K	E_C - 498K	E_C - 698K
R - 0%	~4.53	~3.35	~2.19
M_C - 4%	~5.15	~3.997	~2.91
M_C - 6%	~10.53	~9.38	~8.45

Tables 4.1 and 4.2 displays the range of the coercive fields determined from thermodynamic calculation and phase-field modeling, respectively. At room temperature, the homogeneous electrical fields required to induce switching in the phase-field model are slightly larger than predicted in the analytical model. The phase-field model simulates not only the switching of a single phase to another single phase, but also the switching of single phases to mixed phases, and vice versa. As a result, transition includes the additional energy required to mediate the R/M_C mixed phase boundaries. At room temperature, the phase-field model's first switching

event at 4% strain is between the switching values for the thermodynamic model's R and M_C phases, and its second switching event shows reasonable agreement with the thermodynamic model's M_A phase. Since the phase-field model shows electrical switching from the M_C to the R/M_C mixed phase, as well as momentarily stable R and M_A phases, the thermodynamic model can be used as an estimate for individual switching events that model phase transition, rather than full electrical switching of a single phase. As temperature increases, the coercive fields of both thermodynamic and phase-field models decrease at roughly the same rate.

References

[1] Zhao, T. *et al.* Electrical control of antiferromagnetic domains in multiferroic $BiFeO_3$ films at room temperature. *Nat. Mater.* **5,** 823–829 (2006).

[2] Baek, S. H. *et al.* Ferroelastic switching for nanoscale non-volatile magnetoelectric devices. *Nat. Mater.* **9,** 309–314 (2010).

[3] Nelson, C. T. *et al.* Domain dynamics during ferroelectric switching. *Science (80-.).* **334,** 968–971 (2011).

[4] Beekman, C. *et al.* Phase Transitions, Phase Coexistence, and Piezoelectric Switching Behavior in Highly Strained $BiFeO_3$ Films. *Adv. Mater.* **25,** 5561–5567 (2013).

[5] Catalan, G. & Scott, J. F. Physics and Applications of Bismuth Ferrite. *Adv. Mater.* **21,** 2463–2485 (2009).

[6] Xue, F., Li, Y., Gu, Y., Zhang, J. & Chen, L.-Q. Strain phase separation: Formation of ferroelastic domain structures. *Phys. Rev. B* **94,** 220101 (2016).

[7] Sharma, P. *et al.* Structural and electronic transformation pathways in morphotropic $BiFeO_3$. *Sci. Rep.* **6,** 32347 (2016).

[8] Cao, Y. *et al.* Exploring Polarization Rotation Instabilities in Super-Tetragonal $BiFeO_3$ Epitaxial Thin Films and Their Technological Implications. *Adv. Electron. Mater.* **2,** 1600307 (2016).

[9] Zeches, R. J. *et al.* A Strain-Driven Morphotropic Phase Boundary in $BiFeO_3$. *Science (80-.).* **326,** 977–980 (2009).

[10] Vasudevan, R. K. *et al.* Nanoscale Control of Phase Variants in Strain-Engineered $BiFeO_3$. *Nano Lett.* **11,** 3346–3354 (2011).

[11] Béa, H. *et al.* Evidence for room-temperature multiferroicity in a compound with a giant axial ratio. *Phys. Rev. Lett.* **102,** 1–5 (2009).

[12] Diéguez, O., González-Vázquez, O. E., Wojdeł, J. C. & Íñiguez, J. First-principles predictions of low-energy phases of multiferroic $BiFeO_3$. *Phys. Rev. B* **83,** 094105 (2011).

[13] Liu, H.-J. *et al.* Structural study in highly compressed $BiFeO_3$ epitaxial thin films on $YAlO_3$. *J. Appl. Phys.* **112,** 052002 (2012).

Chapter 5: Conclusions and Future Works

5.1 - Conclusions

In this thesis, thermodynamic calculations and phase-field modeling are applied to study the phase transition and coexistence behavior of ferroelectric BFO with respect to temperature, in-plane compressive strain, and applied electric field. The primary contributions of this thesis include:

1: At room temperature, rhombohedral-like (*R*) BFO is favored at small compressive strains (0%-3% strain), and monoclinically distorted tetragonal (M_A/M_C) BFO is favored for larger compressive strains (>5% strain).

2: Mixed phase BFO consisting of *R* and M_A/M_C BFO exist for strains between 3-5%. The phase amount of R BFO decreases linearly with increasing strain.

3: Increasing temperature shifts the boundaries of the BFO's phases towards higher strains, increasing the stability of *R* BFO at higher compressive strains, and increasing the strain required to stabilize M_A/M_C BFO.

4: The strain window for mixed phase BFO predicted by phase-field simulation is narrower than the window predicted by thermodynamic analysis. This is likely due to the effects of nonlinear strain and the energy required to form domain walls between each phase.

5: At 0% strain, BFO undergoes domain switching between a single R^+ domain and a single R^- domain under bi-polar electrical bias.

6: Under 4% strain from a pure M_C phase, R phase emerge and continue to grow at the domain boundaries during the switching process. The M_C/R mixed phase is stable under an electric field window of ~4.0 (10^8 V/m).

7: At 6% strain, BFO undergoes domain switching between a single M_C^+ phase and a single M_C^- phase under bi-polar electric bias. The bias window for domain switching is narrower than that under 4% strain, and the M_C/R mixed state is a mere transient state during the switching process.

8: Both thermodynamic analysis and phase-field simulation indicate that the coercive field for domain switching decreases as temperature increases under a given state of substrate strain.

5.2 – Future work

5.2.1 – Octahedral tilt

For this theoretical work, the effects of the tilt of the oxygen octahedral in the BFO unit cell are neglected for simplification. However, several studies suggest that it plays a pivotal role in temperature-dependent applications[1], and may be a primary factor in determining phase stability for BFO as well as preferential formation of domain walls[2 3]. As a result, the effects of octahedral tilt will be explored to understand their impact on phase formation in the future.

5.2.2 – Intermediate "S" Phase

Several studies have suggested the rhombohedral phase present in the R/M_C mixture is distinct from its bulk counterpart, with a slightly expanded axial ratio and monoclinic or triclinic symmetry[4 5 6]. The current free energy model of both the thermodynamic and phase-field methods models the Landau energy up to 8^{th} order, which can represent crystal symmetries up to monoclinic symmetry[7]. As a result, the true crystal symmetry of the strained R phase is still uncertain. As a result, reworking the free energy model up to 12^{th} order to accommodate triclinic symmetries may reveal important properties about BFO's phase mixture and morphotropic phase boundaries.

References

[1] Infante, I. C. *et al.* Bridging multiferroic phase transitions by epitaxial strain in $BiFeO_3$. *Phys. Rev. Lett.* **105,** 057601 (2010).

[2] Diéguez, O., González-Vázquez, O. E., Wojdeł, J. C. & Íñiguez, J. First-principles predictions of low-energy phases of multiferroic $BiFeO_3$. *Phys. Rev. B* **83,** 094105 (2011).

[3] Lubk, A., Gemming, S. & Spaldin, N. A. First-principles study of ferroelectric domain walls in multiferroic bismuth ferrite. *Phys. Rev. B - Condens. Matter Mater. Phys.* **80,** 1–8 (2009).

[4] Beekman, C. *et al.* Phase Transitions, Phase Coexistence, and Piezoelectric Switching Behavior in Highly Strained $BiFeO_3$ Films. *Adv. Mater.* **25,** 5561–5567 (2013).

[5] Siemons, W. *et al.* A complete strain–temperature phase diagram for $BiFeO_3$ films on $SrTiO_3$ and $LaAlO_3$ (0 0 1) substrates. *J. Phys. D. Appl. Phys.* **47,** 034011 (2014).

[6] Sando, D., Xu, B., Bellaiche, L. & Nagarajan, V. A multiferroic on the brink: Uncovering the nuances of strain-induced transitions in $BiFeO_3$. *Appl. Phys. Rev.* **3,** 011106 (2016).

[7] Vanderbilt, D. & Cohen, M. H. Monoclinic and triclinic phases in higher-order Devonshire theory. *Phys. Rev. B* **63,** 094108 (2001).

Appendix A

Material Constants of BFO for Thermodynamic Analysis

4^{th} order and above terms from [1]

α_{11}: $(T - 1088)/\varepsilon_0 C$ (C^{-2} m^2 N)

ε_0: 8.85418782 * 10^{-12}

C: 2.5833* 10^5

a_{1111}:2.127*10^9 (C^{-4} m^6 N)

a_{1122}:-2.049*10^9 (C^{-4} m^6 N)

a_{111111}:-1.760*10^9 (C^{-6} m^{10} N)

a_{111122}:8.298*10^8 (C^{-6} m^{10} N)

a_{112233}:1.679*10^9 (C^{-6} m^{10} N)

$a_{11111111}$:3.920*10^8 (C^{-8} m^{14} N)

$a_{11111122}$:4.400*10^7 (C^{-8} m^{14} N)

$a_{11112222}$:-3.800*10^8 (C^{-8} m^{14} N)

$a_{11112233}$:8.000*10^8 (C^{-8} m^{14} N)

h_{1111} =0.07700 (C^{-2} m^4)

h_{1122}=-0.0300 (C^{-2} m^4)

h_{1212}=-0.0007300 (C^{-2} m^4)

c_{1111} = 2.28*10^{11} (N m^{-2})

$c_{1122} = 1.28*10^{11}$ (N m^{-2})

$c_{1212} = 0.65*10^{11}$ (N m^{-2})

κ_B: 50

References

[1] Xue, F., Li, Y., Gu, Y., Zhang, J. & Chen, L.-Q. Strain phase separation: Formation of ferroelastic domain structures. *Phys. Rev. B* **94,** 220101 (2016).

Appendix B

Material Constants of BFO for Phase-Field Modeling

α_{11}: $(T - 1088)/\varepsilon_0 C$ (C^{-2} m^2 N)

ε_0: 8.85418782 * 10^{-12}

C: 2.5833* 10^5

α_{1111}: 2.12724356*10^9 (C^{-4} m^6 N)

α_{1122}: -2.049415*10^9 (C^{-4} m^6 N)

α_{111111}:-1.76*10^9 (C^{-6} m^{10} N)

$\alpha_{111122:}$ 8.29814*10^8(C^{-6} m^{10} N)

α_{112233}:1.67944*10^9 (C^{-6} m^{10} N)

$\alpha_{11111111}$:3.920*10^8 (C^{-8} m^{14} N)

$\alpha_{11111122}$:4.4*10^7 (C^{-8} m^{14} N)

$\alpha_{11112222}$: -3.8*10^8 (C^{-8} m^{14} N)

$\alpha_{11112233}$:8.0*10^8 (C^{-8} m^{14} N)

h_{1111}:0.07700 (C^{-2} m^4)

h_{1122}:-0.03 (C^{-2} m^4)

h_{1212}: 0.0215 (C^{-2} m^4)

c_{1111}:2.28*10^{11}

c_{1122}:1.28*10^{11}

c_{1212}:0.65*10^{11}

G_{11}: $4.335*10^{-11}$

G_{44}: $0.34*10^{-11}$

G_{44}': $0.34*10^{-11}$

κ_B: 50

Appendix C

Mathematica Code for Thermodynamic analysis

C.1: Polarization and Helmholtz Free energy analysis – Single Phase

h11 = h12 = h13 = h14 = h15 = h16 = 0
h21 = h22 = h23 = h24 = h25 = h26 = 0
h31 = h32 = h33 = h34 = h35 = h36 = 0
h41 = h42 = h43 = h44 = h45 = h46 = 0
h51 = h52 = h53 = h54 = h55 = h56 = 0
h61 = h62 = h63 = h64 = h65 = h66 = 0

c11 = c12 = c13 = c14 = c15 = c16 = 0
c21 = c22 = c23 = c24 = c25 = c26 = 0
c31 = c32 = c33 = c34 = c35 = c36 = 0
c41 = c42 = c43 = c44 = c45 = c46 = 0
c51 = c52 = c53 = c54 = c55 = c56 = 0
c61 = c62 = c63 = c64 = c65 = c66 = 0

c12 = c21
c13 = c31
c14 = c41
c15 = c51
c16 = c61
c23 = c32
c24 = c42
c25 = c52
c26 = c62
c34 = c43
c35 = c53
c36 = c63
c45 = c54
c46 = c64
c56 = c65

P1 = Px (*C/m^2*)
P2 = Py
P3 = Pz
a11 = 1.093*(T - 815 - 273)*10^5*4
a1111 = 2.127*10^9 (*C^-4 m^6 N*)
a1122 = -2.049*10^9 (*C^-4 m^6 N*)
a111111 = -1.760*10^9 (*C^-6 m^10 N*)
a111122 = 8.298*10^8 (*C^-6 m^10 N*)
a112233 = 1.679*10^9 (*C^-6 m^10 N*)
a11111111 = 3.920*10^8 (*C^-8 m^14 N*)
a11111122 = 4.400*10^7 (*C^-8 m^14 N*)
a11112222 = -3.800*10^8 (*C^-8 m^14 N*)
a11112233 = 8.000*10^8 (*C^-8 m^14 N*)
h11 = h22 = h33 = 0.07700 (*C^-2 m^4*)
h12 = -0.0300 (*C^-2 m^4*)

```
h44 = h55 = h66 = -0.0007300 (*C^-2 m^4*)
g11 = 4.335*10^-11 (*C^-2 m^4 N*)
g12 = -3.400*10^-12 (*C^-2 m^4 N*)
g66 = 3.4*10^-12 (*C^-2 m^4 N*)
c11 = c22 = c33 = 2.28*10^11 (*N m^-2*)
c12 = 1.28*10^11  (*N m^-2*)
c44 = c55 = c66 = 0.65*10^11  (*N m^-2*)
c13 = c23 = c3= c31 = c21 = c12
h13 = h23 = h32 = h31 = h21 = h12

(*Tensors*)
e1t0 = h11*P1^2 + h12*P2^2 + h13*P3^2 + 2*h14*(P2*P3) +
  2*h15*(P1*P3) + 2*h16*(P1*P2)
e2t0 = h21*P1^2 + h22*P2^2 + h23*P3^2 + 2*h24*(P2*P3) +
  2*h25*(P1*P3) + 2*h26*(P1*P2)
e3t0 = h31*P1^2 + h32*P2^2 + h33*P3^2 + 2*h34*(P2*P3) +
  2*h35*(P1*P3) + 2*h36*(P1*P2)
e4t0 = h41*P1^2 + h42*P2^2 + h43*P3^2 + 2*h44*(P2*P3) +
  2*h45*(P1*P3) + 2*h46*(P1*P2)
e5t0 = h51*P1^2 + h52*P2^2 + h53*P3^2 + 2*h54*(P2*P3) +
  2*h55*(P1*P3) + 2*h56*(P1*P2)
e6t0 = h61*P1^2 + h62*P2^2 + h63*P3^2 + 2*h64*(P2*P3) +
  2*h65*(P1*P3) + 2*h66*(P1*P2)

s1 = c11*(e1 - e1t0) + c12*(e2 - e2t0) + c13*(e3 - e3t0) +
  c14*(e4 - e4t0) + c15*(e5 - e5t0) + c16*(e6 - e6t0)
s2 = c21*(e1 - e1t0) + c22*(e2 - e2t0) + c23*(e3 - e3t0) +
  c24*(e4 - e4t0) + c25*(e5 - e5t0) + c26*(e6 - e6t0)
s3 = c31*(e1 - e1t0) + c32*(e2 - e2t0) + c33*(e3 - e3t0) +
  c34*(e4 - e4t0) + c35*(e5 - e5t0) + c36*(e6 - e6t0)
s4 = c41*(e1 - e1t0) + c42*(e2 - e2t0) + c43*(e3 - e3t0) +
  c44*(e4 - e4t0) + c45*(e5 - e5t0) + c46*(e6 - e6t0)
s5 = c51*(e1 - e1t0) + c52*(e2 - e2t0) + c53*(e3 - e3t0) +
  c54*(e4 - e4t0) + c55*(e5 - e5t0) + c56*(e6 - e6t0)
s6 = c61*(e1 - e1t0) + c62*(e2 - e2t0) + c63*(e3 - e3t0) +
  c64*(e4 - e4t0) + c65*(e5 - e5t0) + c66*(e6 - e6t0)
Eelastic = 0.5*(s1*(e1 - e1t0) + s2*(e2 - e2t0) + s3*(e3 - e3t0) +
    s4*(e4 - e4t0) + s5*(e5 - e5t0) + s6*(e6 - e6t0))

Landau2nd = a11*(Px^2 + Py^2 + Pz^2)
Landau4th = a1111*(Px^4 + Py^4 + Pz^4) +  a1122*((Px^2*Py^2) + (Py^2*Pz^2) + (Px^2*Pz^2))
Landau6th = a111111*(Px^6 + Py^6 + Pz^6) +  a111122*(Px^4*(Py^2 + Pz^2) + Py^4*(Pz^2 +
Px^2) + Pz^4*(Px^2 + Py^2)) + a112233*(Px^2*Py^2*Pz^2)
Landau8th = a11111111*(Px^8 + Py^8 + Pz^8) +
a11111122*(Px^6*(Py^2 + Pz^2) + Py^6*(Px^2 + Pz^2) + Pz^6*(Px^2 + Py^2)) +
a11112222*(Px^4*Py^4 + Py^4*Pz^4 + Px^4*Pz^4) +
```

```
a11112233*(Px^4*Py^2*Pz^2 + Py^4*Px^2*Pz^2 + Pz^4*Px^2*Py^2)
Landau = Landau2nd + Landau4th + Landau6th + Landau8th

eps0 = 8.854*10^-12 (* F/m OR C/(V m) *)
Kb1 = Kb2 = Kb3 = 50 (*Dimensionless *)
eps11 = eps0*Kb1
eps12 = eps0*Kb2
eps13 = eps0*Kb3
Eelec = -(EfieldX*Px + EfieldY*Py + EfieldZ*Pz) -
  1/2 *(eps11*EfieldX^2 + eps11*EfieldY^2  + eps11*EfieldZ^2)

hFree = Landau + Eelec + Eelastic
dhdx = D[hFree, Px]
dhdy = D[hFree, Py]
dhdz = D[hFree, Pz]

d2hdx = D[hFree, {Px, 2}]
d2hdy = D[hFree, {Py, 2}]
d2hdz = D[hFree, {Pz, 2}]

dhde1 = D[hFree, e1]
dhde2 = D[hFree, e2]
dhde3 = D[hFree, e3]
dhde4 = D[hFree, e4]
dhde5 = D[hFree, e5]
dhde6 = D[hFree, e6]
d2hde1 = D[hFree, {e1, 2}]
d2hde2 = D[hFree, {e2, 2}]
d2hde3 = D[hFree, {e3, 2}]
d2hde4 = D[hFree, {e4, 2}]
d2hde5 = D[hFree, {e5, 2}]
d2hde6 = D[hFree, {e6, 2}]
```

$$\text{For}[i = 1, i \leq 10, i{+}{+}, \text{Print}[\text{TableForm}[\text{sol} = \text{NSolve}[\text{dhdx} == 0 \&\& \text{dhdy} == 0 \&\& \text{dhdz} == 0 \&\& \text{d2hdx} \geq 0 \&\& \text{d2hdy} \geq 0 \&\& \text{d2hdz} \geq 0 \&\& \text{e6} == 0 \&\& \text{dhde5} = = 0 \&\& \text{dhde4} == 0 \&\& \text{dhde3} == 0 \&\& \text{e2} == \text{e1} = = -((i-1) * 0.002 + 0.046) \&\& \text{EfieldX} == 0 \&\& \text{EfieldY} == 0 \&\& \text{Px} \geq 0 \&\& \text{Py} \geq 0 \&\& \text{EfieldZ} == (-000000000) \&\& T = = 598, \{T, \text{Px}, \text{Py}, \text{Pz}, \text{e1}, \text{e2}, \text{e3}, \text{e4}, \text{e5}, \text{e6}, \text{EfieldX}, \text{EfieldY}, \text{EfieldZ}\}, \text{Reals}]]];$$
$$\text{Print}[\text{Dimensions}[\text{sol}]]; \text{Print}[\text{Column}[\text{hFree}/.\text{sol}]];]$$

C.2 Mathematica Code – Phase Mixture and Critical Strain analysis

```
y1 = 128400551033.02 x^2 + 14292916552.99 x + 718756665.14
y2 = 168813785478.88 x^2 - 1457526488.09 x - 78704180.87
fy1 = (128400551033.02 #^2 + 14292916552.99 # + 718756665.14) &
```

```
fy2 = (168813785478.88 #^2 - 1457526488.09 # - 78704180.87) &
dy1 = D[y1, x]
dy2 = D[y2, x]
fdy1 = (1.429291655299`*^10 + 2.5680110206604`*^11 #) &
fdy2 = (-1.45752648809`*^9 + 3.3762757095776`*^11 #) &
Tangent = m*x + c
fTan = (m # + c) &
NSolve[fy1[x1] == fTan[x1] && fy2[x2] == fTan[x2] && fdy1[x1] == fdy2[x2] == m, {m, c, x1,
x2}]
Tan298 = Tangent /. {m -> -6.398846578233712`*^9,  c -> -1.1486331942019928`*^8}
(*Values used for m and c are from previously used NSolve, need to be input manually *)
sTan298 = (-1.1486331942019928`*^8 - 6.398846578233712`*^9  #) &
NSolve[fy1[x1] == sTan698[x1], x1]
NSolve[fy2[x1] == sTan698[x1], x1]
```

Biographical Information

Ryan Thomas Hart was born in Fort Bragg, North Carolina on April 8th, 1994. He grew up as an army brat, living in several different cities before his family settled in Arlington, Texas. He graduated high school in 2012, and graduated with a Bachelor of Science in Mechanical Engineering from the University of Texas at Arlington in December 2016. The author then joined the University of Texas at Arlington's Department of Materials Science and Engineering to conduct graduate studies as a master's student, first researching under Dr. Perena Gouma, then Dr. Ye Cao. The author's current research interests include additive manufacturing, computational materials analysis, and materials for energy storage.